MITP/16-023

Angular observables for spin discrimination in boosted diboson final states

Malte Buschmann* and Felix Yu†

PRISMA Cluster of Excellence & Mainz Institute for Theoretical Physics,

Johannes Gutenberg University, 55099 Mainz, Germany

We investigate the prospects for spin determination of a heavy diboson resonance using angular observables. Focusing in particular on boosted fully hadronic final states, we detail both the differences in signal efficiencies and distortions of differential distributions resulting from various jet substructure techniques. We treat the 2 TeV diboson excess as a case study, but our results are generally applicable to any future discovery in the diboson channel. Scrutinizing ATLAS and CMS analyses at 8 TeV and 13 TeV, we find that the specific cuts employed in these analyses have a tremendous impact on the discrimination power between different signal hypotheses. We discuss modified cuts that can offer a significant boost to spin sensitivity in a post-discovery era. Even without altered cuts, we show that CMS, and partly also ATLAS, will be able to distinguish between spin 0, 1, or 2 new physics diboson resonances at the 2σ level with 30 fb^{-1} of 13 TeV data, for our 2 TeV case study.

arXiv:1604.06096v2 [hep-ph] 10 Feb 2017

* buschmann@uni-mainz.de

† yu001@uni-mainz.de

CONTENTS

I. Introduction 2

II. Reconstructing Angular Correlations in $pp \to X$, $X \to V_1V_2 \to 4q$ 6

A. General framework 6

B. Phenomenology of jet substructure 7

III. Angular observables in the $4q$ final state: the 2 TeV case study 11

A. Signal benchmarks 11

B. ATLAS and CMS analysis cuts at 8 TeV and 13 TeV 12

C. Analysis effects and reconstruction 14

IV. Angular observables in semi-leptonic final states 23

A. ATLAS and CMS semi-leptonic analyses at 8 TeV and 13 TeV 24

B. Angular observables in semi-leptonic final states and comparison with fully hadronic final states 27

V. Projections for model discrimination from $4q$ final state 31

VI. Conclusion 35

Acknowledgments 36

A. ATLAS 13 TeV background extraction, inclusive diboson selection 36

References 37

I. INTRODUCTION

The resumption of the Large Hadron Collider (LHC) with proton-proton collisions at 13 TeV has reignited the excitement for a possible discovery of new physics. The higher energies afforded by the increase in energy during Run 2 also place additional importance on the need for robust analysis tools to enable such discoveries in the hadronic enviroment of the LHC. One such suite of analysis techniques is the maturing field of jet substructure [1–5], which take advantage of large Lorentz boosts of decaying Standard Model (SM) or new physics (NP) particles to reveal their

underlying partonic constituents. Jet substructure tools are also invaluable for mitigating pile-up backgrounds at the LHC, allowing the ATLAS and CMS experiments to use primary vertex information and jet substructure methods to discard pile-up contamination of jets resulting from the hard scattering process of interest [6, 7].

The special utility of jet substructure techniques as new physics discovery tools was recently highlighted in the ATLAS 8 TeV search for electroweak diboson resonances in fully hadronic final states [8]. In this analysis, ATLAS observed a 2.5σ global significance deviation at about 2 TeV in the reconstructed WZ invariant mass distribution. The corresponding CMS 8 TeV analysis [9] does not preclude a possible signal at ATLAS, partly because the two experiments use different reconstruction methods for tagging boosted, hadronically decaying W and Z candidates. The most recent 13 TeV results from ATLAS [10] and CMS [11] in the same fully hadronic diboson decay, however, show no evidence for a continued excess.

If the excess is a new physics signal, numerous studies are needed to characterize the resonance and measure the underlying new physics Lagrangian. First, for self-consistency, the signal must also begin to show up in the semi-leptonic and fully leptonic diboson decays. Observing the excess in these decays is also critical, though, because the exclusive rates for the semi-leptonic and fully leptonic modes will help diagnose the underlying W^+W^- vs. $W^\pm Z$ vs. ZZ nature of the purported resonance, which is difficult to disentangle using only hadronic diboson decays. Currently, ATLAS has searches for electroweak diboson resonances with 8 TeV data in the $\ell\nu\ell\ell$ channel [12], $\ell\ell jj$ channel [13], and the $\ell\nu jj$ channel [14], which have been combined with the fully hadronic search in Ref. [15]. In addition, CMS has searches with 8 TeV data in the $\ell\nu\ell\ell$ channel [16] and $\ell\nu jj$ and $\ell\ell jj$ channels [17]. We remark, however, that the 2 TeV excess seen by ATLAS in the fully hadronic channel is only marginally probed by the analyses targetting semi-leptonic diboson decays, after rescaling the signals that fit the excess by the appropriate leptonic branching fractions [18].

The current situation with 13 TeV data seems to favor the interpretation that the 2 TeV excess was instead a statistical fluctuation, although the data is not conclusive. Both ATLAS and CMS have retooled their fully hadronic diboson resonance analyses [10, 11] to focus on the multi-TeV regime, adopting different jet substructure methods than those used previously during the 8 TeV run. CMS and ATLAS also search in the $\ell\nu jj$ channel [11, 19], respectively, and ATLAS also has performed analyses in the $\ell\ell jj$ channel [20] as well as the $\nu\nu jj$ channel [21]. Although the integrated luminosity at 13 TeV is only 3.2 fb^{-1} for ATLAS and 2.6 fb^{-1} for CMS, in comparison to the 20 fb^{-1} datasets for each experiment at 8 TeV, naive parton luminosity rescaling from 8 TeV to 13 TeV for the simplest new physics explanations of the 2 TeV excess point to ATLAS and

CMS being at the edge of NP exclusion sensitivity (see Figure 8 of [10], Figure 4 of [19], Figure 4 of [21], and Figures 9 and 10 of [11]).

Beyond the self-consistency requirement to observe the diboson excess in leptonic channels, various new physics models also predict a new dijet resonance as well as VH resonances, where V is a massive electroweak boson and H is the Higgs boson [22–26]. The corresponding dijet resonance searches from ATLAS 8 TeV data [27], CMS 8 TeV data [28], ATLAS 13 TeV data [29] and CMS 13 TeV data [30], as well as WH and ZH resonance searches with 8 TeV ATLAS data [31], 8 TeV CMS data [32–34], and 13 TeV ATLAS data [35], have all variously been statistically consistent with the SM background expectation, which then provide important model-dependent constraints on new physics interpretations of the 2 TeV excess.

Given the experimental situation, many papers have delved into the model-building details and phenomenological questions that reconcile the original excess with the currently available experimental data. Spin-0 explanations are discussed in context of a Higgs singlet [36], a two Higgs doublet model [37–40], sparticles [41, 42] or composite scalars [43, 44]. Spin-1 proposals include composite vector resonances [45–52], generic and effective field theory (EFT) models [53–56] as well as heavy W' resonances [22–25, 57–69], Z' resonances [26, 70–76] or both [77–83]. Other NP scenarios include glueballs [84], excited composite objects [85], and in generic and EFT models [86–91].

Although the new physics situation with 13 TeV data is less attractive because the initial dataset does not confirm the excess, the experimental sensitivity with the current luminosity is nonetheless insufficient to make a final conclusion for the original excess. Thus the question about whether the excess is a real signal will simply have to wait for more integrated luminosity.

Apart from the excitement over the original ATLAS diboson excess, however, we are motivated to consider how jet substructure techniques can be used as post-discovery tools for resonance signal discrimination. After the Higgs discovery in 2012, the ATLAS and CMS collaborations began comprehensive Higgs characterization programs, which aim to measure the couplings, mass, width, spin, parity, production modes, and decay modes of the Higgs boson. In particular, much of the spin and parity information about the 125 GeV Higgs boson comes from angular correlations in the $h \to 4\ell$ decay [92–95], where the Higgs candidate can be fully reconstructed and all angular observables can be studied.

For the case of a possible 2 TeV resonance X, the exact same analytic formalism for spin characterization used for $h \to 4\ell$ [96–101] applies to $X \to VV \to 4q$ [87], which naturally opens up the possibility of designing a jet substructure analysis that targets spin and possibly parity character-

ization of the X resonance. The $X \to VV \to 4q$ situation is more difficult, however, because it is a priori unknown how well the angular correlations in the final state quarks are preserved after the important effects from showering and hadronization, detector resolution, jet clustering, and hadronic W and Z boson tagging are included. In contrast, the $h \to 4\ell$ decay can be analyzed without the complications from quantum chromodynamics (QCD) and only need to account for virtual γ^*/Z interference and mild detector effects [102–104]. Our study provides a thorough investigation of these important and difficult complications, and we connect distortions in angular observables with specific jet substructure cuts. Our results show significant differences between the ATLAS and CMS 8 TeV and 13 TeV analyses regarding post-discovery signal discrimination. They also provide useful templates for understanding the differences in sensitivity of the current jet substructure methods to tranversely or longitudinally polarized electroweak gauge bosons. We also make projections for how well the current slate of diboson reconstruction methods will perform with 30 fb^{-1} of LHC 13 TeV integrated luminosity. The next obvious course of action would be to design a jet substructure method optimized for both signal significance and post-discovery spin discrimination using the extracted subjets. We leave such work for the future and instead focus on determining the viability of existing jet substructure techniques with regards to spin determination.

In Section II, we review the angular analysis framework for characterizing a resonance decay. We also review the broad classes of jet substructure methods and general challenge of reconstructing angular correlations in the fully hadronic final state and the hadronic environment. In Section III, we detail the 2 TeV case study signal benchmarks, review the 8 TeV and 13 TeV ATLAS and CMS fully hadronic boosted diboson decay selection criteria, and show the differential distributions after implementing these analyses. We also identify specific jet substructure cuts to their effects on the differential distributions. We evaluate the semileptonic analyses in Section IV in a similar manner, highlighting the new distortions that arise when considering semileptonic final states. We present our expectations for model discrimination with 30 fb^{-1} of LHC 13 TeV data in Section V and briefly discuss improvements in jet substructure analyses targetting signal discrimination. We conclude in Section VI. In Appendix A, we discuss the inclusive background determination for the ATLAS 13 TeV analysis neeeded in our 13 TeV, 30 fb^{-1} projections.

II. RECONSTRUCTING ANGULAR CORRELATIONS IN $pp \to X$, $X \to V_1V_2 \to 4q$

A. General framework

In this section, we review the general framework for studying angular correlations of a resonance X decaying to two intermediate vector bosons that subsequently decay to four light quarks. We will work in the X rest frame and orient the incoming partons along the $+\hat{z}$ and $-\hat{z}$ axes as usual. We also neglect the masses of our final state particles, which reduces the nominal sixteen final state four-momentum components to twelve. Four-momentum conservation in the rest frame of the resonance further reduces the number of independent components to eight. Finally, the overall system can be freely rotated about the $+\hat{z}$ axis, so we can completely characterize the kinematics of the system with seven independent variables, which are five angles and the two intermediate vector masses. If the resonance mass is not known, it also counts as an independent quantity. Finally, if the final state particles are not massless, then their four masses also have to be used as independent variables.

The five angles, known as the Cabibbo–Maksymowicz–Dell'Aquila–Nelson angles [96–99], the two intermediate vector masses, and the resonance mass are hence completely sufficient to describe the kinematics of the $pp \to X \to V_1V_2 \to (p_1p_2)(p_3p_4)$. These angles are shown in Fig. 1 and are given by

$$\begin{aligned} \cos\theta_{p_1} &= -\hat{p}_{p_1} \cdot \hat{p}_{V_2} \ , & \Phi_{V_1} &= \frac{\vec{p}_{V_1} \cdot (\hat{n}_1 \times \hat{n}_{\text{sc}})}{|\vec{p}_{V_1} \cdot (\hat{n}_1 \times \hat{n}_{\text{sc}})|} \arccos(\hat{n}_1 \cdot \hat{n}_{\text{sc}}) \ , \\ \cos\theta_{p_3} &= -\hat{p}_{p_3} \cdot \hat{p}_{V_1} \ , & \Phi &= \frac{\vec{p}_{V_1} \cdot (\hat{n}_1 \times \hat{n}_2)}{|\vec{p}_{V_1} \cdot (\hat{n}_1 \times \hat{n}_2)|} \arccos(-\hat{n}_1 \cdot \hat{n}_2) \ , \\ \cos\theta^* &= \hat{p}_{V_1} \cdot \hat{z}_{\text{beam}} \ , \end{aligned} \tag{1}$$

where V_1 and V_2 are the two bosons, X is the resonance, $\hat{z}_{\text{beam}}$ is the direction of the beam axis and

$$\hat{n}_1 = \frac{\vec{p}_{p_1} \times \vec{p}_{p_2}}{|\vec{p}_{p_1} \times \vec{p}_{p_2}|} \ , \quad \hat{n}_2 = \frac{\vec{p}_{p_3} \times \vec{p}_{p_4}}{|\vec{p}_{p_3} \times \vec{p}_{p_4}|} \ , \text{ and } \hat{n}_{\text{sc}} = \frac{\hat{z}_{\text{beam}} \times \vec{p}_{p_1}}{|\hat{z}_{\text{beam}} \times \vec{p}_{p_1}|} \ . \tag{2}$$

The intermediate vectors V_1 and V_2 are reconstructed by $p_{V_1} = p_{p_1} + p_{p_2}$, $p_{V_2} = p_{p_3} + p_{p_4}$, and the resonance X is formed by $p_X = p_{V_1} + p_{V_2}$. The angle $\cos\theta_{p_1}$ ($\cos\theta_{p_3}$) is calculated with the respective four-momenta boosted into the rest frame of particle V_1 (V_2), whereas all other angles are computed in the rest frame of particle X. Additionally, we define the angle $\Psi = \Phi_{V_1} + \Phi/2$ to supersede Φ_{V_1}, where Ψ is the average azimuthal angle of the two decay planes.

Resonances with different spins will produce different angular correlations among the decay products. A full set of analytic expressions for different resonance hypotheses and the subsequent

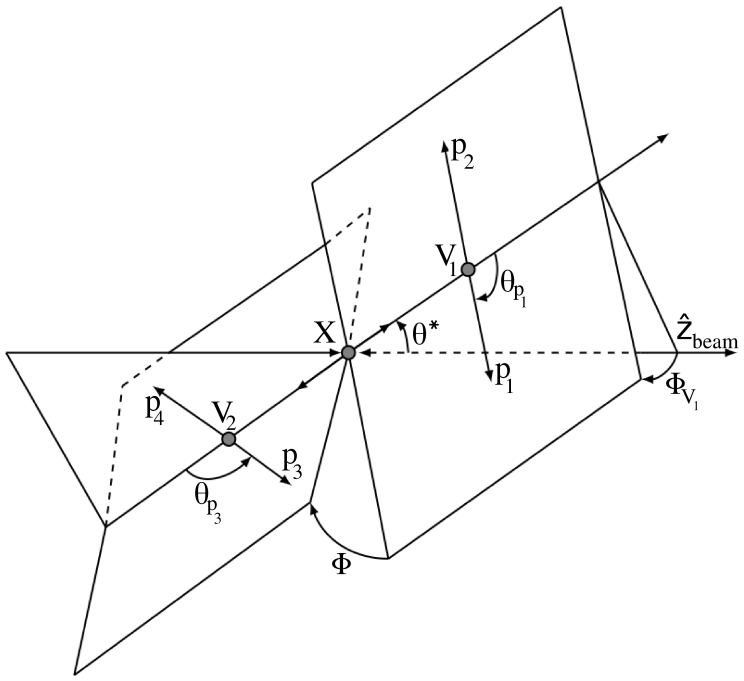

FIG. 1. Representation of the Cabibbo–Maksymowicz–Dell'Aquila–Nelson angles defined in Eq. 1.

angular correlations in the $X \to V_1V_2 \to 4$ fermion final state can be found in Ref. [101], which we do not reproduce here. We have verified the analytic expressions in Ref. [101] by comparing to parton level Monte Carlo results for different resonant spin hypotheses. Our full discussion of Monte Carlo signal samples and analysis of angular correlations analysis is given in Section III.

B. Phenomenology of jet substructure

While the angles defined in Fig. 1 underpin any analysis aimed at spin characterization of a given resonance, the corresponding differential distributions are expected to be smeared and skewed after accounting for showering and hadronization, detector resolution effects, jet clustering methods, and jet substructure cuts. Of these effects, the distortions introduced by jet clustering methods and jet substructure cuts are the most pernicious.

The usual goal for jet substructure techniques is to isolate the partonic constituents of a given wide angle jet that captures the decay products of a boosted parent, like a W, Z, h, or t resonance. As a result, different methods have been developed to maximize the tagging efficiency of these parent particles while simultaneously minimizing the mistag rate from QCD or other backgrounds [3, 4]. In this endeavor, angular observables have played an implicit role to help improve

the overall tagging efficiency of a given parent particle over the QCD background, but on the other hand, recovering the full phase space of resonance decay products will be key for post-discovery signal discrimination. Moreover, understanding how angular observables are distorted by jet substructure cuts is also necessary to optimize signal hypothesis testing in a post-discovery scenario.

To this end, we review the main jet substructure methods to extract subjets from fat jets, as well as jet substructure techniques used for background discrimination. Variants of these methods are all used, as we will see, in the most recent ATLAS and CMS 8 TeV and 13 TeV analyses [8–11].

Mass-drop filter technique

The jet grooming procedure used in the 8 TeV ATLAS analysis [8] is known as mass-drop filtering [1]. An original fat jet, reconstructed with the Cambridge-Aachen (C/A) cluster algorithm [105], is "unclustered" in reverse order. Each step of the unclustering gives a pair of subjets that is tested for both mass-drop and momentum balance conditions. The procedure is stopped if the two conditions are satisfied.

The mass-drop criterion requires each subjet to satisfy $\mu_i \equiv m_i/m_0 \leq \mu_f$ for a given parameter μ_f, where m_i is the subjet mass and m_0 is the original jet mass. The 8 TeV ATLAS hadronic and semi-leptonic diboson searches use $\mu_f = 1$, which effectively means no mass-drop cut is applied.

The subjet momentum balance condition imposes a minimum threshold on the relative p_T and ΔR of each subjet, according to

$$\sqrt{y} = \min(p_{T_1},\ p_{T_2})\frac{\Delta R}{m_0} \geq \sqrt{y_{\min}}\ , \tag{3}$$

where p_{T_i} is the transverse momentum of each subjet j_i, $\Delta R = \sqrt{(\Delta\phi)^2 + (\Delta\eta)^2}$ is their angular distance, and $\sqrt{y_{\min}}$ is a parameter controlling the threshold. To see how Eq. (3) acts as a cut on the subjet momentum balance, we rewrite Eq. (3) using

$$m_0^2 = 2p_{T_1}p_{T_2}\left(\cosh(\Delta\eta) - \cos(\Delta\phi)\right) \approx p_{T_1}p_{T_2}(\Delta R)^2\ , \tag{4}$$

which holds as long as the rapidity difference $\Delta\eta$ and azimuthal separation $\Delta\phi$ are small. Using this approximation, we see that the $\sqrt{y_{\min}}$ cut is indeed a subjet momentum balance cut as advertised,

$$y \approx \frac{\{\ \min(p_{T_1},\ p_{T_2})\}^2}{p_{T_1}p_{T_2}} = \frac{p_{T,\ \min}}{p_{T,\ \max}} \geq y_{\min}\ . \tag{5}$$

At each stage of the unclustering, if the pair of subjets under consideration satisfies $\sqrt{y} \geq \sqrt{y_{\min}}$, the procedure terminates and the total four-momentum of the subjets are used as the W or Z boson candidate. If the subjets fail the cut, the softer subjet is discarded and the unclustering

procedure continues.

Pruning

In contrast to mass-drop filtering, which recursively compares subjets to the original fat jet kinematics, the jet pruning method [106, 107], which is used in the 8 TeV CMS analysis [9], tests each stage of the reclustering for sufficient *hardness* and discards soft recombinations. In this way, each stage of the reclustering offers an opportunity to remove constituents from the final jet, instead of simply incorporating the soft contamination into the widest subjets.

Concretely, in the jet pruning method, the constituents of a fat jet are reclustered using the C/A algorithm if they are sufficiently balanced in transverse momentum and sufficiently close in ΔR. The transverse momentum balance condition is dictated by a minimum requirement on the *hardness* z, defined by

$$z = \min\left(\frac{p_{T_i}}{p_{T_p}}, \frac{p_{T_j}}{p_{T_p}}\right) , \tag{6}$$

where p_{T_p} is the sum of the tranverse momentum of the psuedojets i and j. Note that z is related the momentum fraction y from Eq. (5) via

$$y \approx \frac{p_{T,\,\mathrm{min}}}{p_{T,\,\mathrm{max}}} = \frac{z}{1-z} . \tag{7}$$

In addition to having sufficient hardness, the two pseudojets must also be closer in ΔR than a parameter D_{cut}, given by

$$\Delta R_{ij} > D_{\mathrm{cut}} \equiv \frac{m_{\mathrm{orig}}}{p_{T,\,\mathrm{orig}}} , \tag{8}$$

where m_{orig} and $p_{T,\,\mathrm{orig}}$ are the invariant mass and transverse momentum of the original fat jet. If either the hardness or the ΔR cut fails, then the softer p_T pseudojet is discarded. The C/A reclustering procedure continues until all the constituents of the original fat jet are included or discarded.

N-subjettiness

The N-subjettiness variable [108, 109] is used by CMS in their 8 TeV and 13 TeV analyses [9, 11] to help suppress QCD multi-jet backgrounds and improve selection of hadronic W and Z candidates. The N-subjettiness is defined as

$$\tau_N = \frac{1}{d_0}\sum_k p_{T_k} \min(\Delta R_{1,k}, \ldots, \Delta R_{N,k}) , \tag{9}$$

where p_{T_k} is the transverse momentum of the kth constituent of the original jet and $\Delta R_{n,k}$ is the angular distance to the nth subjet axis. The set of N subjets is determined by reclustering

all jet constituents of the unpruned jet with the k_T algorithm and halting the reclustering when N distinguishable pseudojets are formed. Here, $d_0 \equiv \sum_k p_{T_k} R_0$ is a normalization factor for τ_N, where R_0 is the cone size of the original fat jet. For the boosted hadronic W and Z analyses, the ratio $\tau_{21} = \tau_2/\tau_1$ is computed, where the signal W and Z candidates tend toward lower τ_{21} values, whereas the QCD background peaks at higher values.

Trimming

The 13 TeV ATLAS analysis [10] was reoptimized for multi-TeV scale diboson sensitivity and adopts the trimming procedure [110] instead of the earlier mass-drop filtering technique. Trimming takes a large radius fat jet and reclusters the constituents with the k_T cluster algorithm [111] using distance parameter $R = 0.2$. Of the resulting set of subjets, those kept must satisfy

$$\frac{p_{T_j}}{p_{T_J}} > z_{\min} \ , \tag{10}$$

where j denotes the subjet and J the original fat jet. The four-momentum sum of all remaining subjets is used as a W or Z candidate. For an ideal W or Z decay, with exactly two final subjets, the above condition translate directly to the same balance criteria as the filtering technique,

$$y \approx \frac{p_{T,\,\min}}{p_{T,\,\max}} \geq y_{\min} = \frac{z_{\min}}{1 - z_{\min}} \ . \tag{11}$$

Note, however, that this algorithm does not consider pairs of subjets as the pruning or filtering techniques do. Thus, it is possible to obtain more than two subjets and hence additional cuts, such as energy correlation function cuts, are needed to determine whether the trimmed jet has a two-prong substructure.

Energy Correlation Functions

The ATLAS 13 TeV analysis [10] uses energy correlation functions [112–114] to characterize the number of hard subjets in their set of trimmed jets. The relevant 1-point, 2-point and 3-point energy correlation functions are

$$\begin{aligned} e_1^{(\beta)} &= \sum_{1 \leq i \leq n_J} p_{T_i} \ , \\ e_2^{(\beta)} &= \sum_{1 \leq i < j \leq n_J} p_{T_i} p_{T_j} \Delta R_{ij}^{\beta} \ , \\ e_3^{(\beta)} &= \sum_{1 \leq i < j < k \leq n_J} p_{T_i} p_{T_j} p_{T_k} \Delta R_{ij}^{\beta} \Delta R_{ik}^{\beta} \Delta R_{jk}^{\beta} \ , \end{aligned} \tag{12}$$

where the sums are performed over jet constituents and β is a parameter weighting the angular separations of constituents against their p_T fractions. Since the sums are performed over jet constituents, the energy correlation functions are independent of any jet algorithm. An upper limit is set on the ratio of the function

$$D_2^{(\beta)} = \frac{e_3^{(\beta)} \left(e_1^{(\beta)}\right)^3}{\left(e_2^{(\beta)}\right)^3} \ , \tag{13}$$

where the ATLAS collaboration uses $\beta = 1$ in their 13 TeV analysis.

III. ANGULAR OBSERVABLES IN THE $4q$ FINAL STATE: THE 2 TEV CASE STUDY

A. Signal benchmarks

We consider spin-0, spin-1 W', spin-1 Z', spin-1 W_R, and spin-2 new physics resonances as possible candidates for the 2 TeV excess from the ATLAS 8 TeV analysis [8]. The spin-0 possibility is an ad-hoc real scalar model built from the Universal FeynRules Output [115] implementation of the SM Higgs effective couplings to gluons in MadGraph v.1.5.14 [116], and is included only as an example of a heavy real scalar that couples dominantly to longitudinal vector bosons. The spin-1 W' and spin-1 Z' possibilities are based on the Heavy Vector Triplet model [47, 117], whose phenomenology related to the ATLAS 2 TeV diboson excess was described in detail in Ref. [47]. The spin-1 W_R explanation is taken from the UFO model files that accompany Ref. [25]. The spin-2 heavy graviton resonance is adapted from a Randall-Sundrum scenario [118, 119] as a MadGraph model file implementation [120].

Each of these signal possibilities is generated as an on-shell resonance in MadGraph with subsequent decays to massive electroweak diboson and then final state SM fermions. These parton level events are then showered and hadronized with Pythia v.8.2 [121], processed through Delphes v.3.1 [122] for detector simulation, and clustered into jets using the FastJet v.3.1.0 [123] as each ATLAS or CMS analysis requires. Because Delphes does not include parametrized detector simulation of jet constituents, which are the basis for studying jet substructure and angular correlations between subjets, we also post-process the jet constituents to smear their p_T, ϕ, and η to mimic detector resolution effects: the constituent smearing parameters are rescaled by the respective energy fraction of the constituent compared to the full jet.

We simulate QCD dijet background with Pythia v.8.2 [121]. The subsequent event evolution is the same as described above.

B. ATLAS and CMS analysis cuts at 8 TeV and 13 TeV

We recast the ATLAS and CMS searches for heavy resonances with hadronic diboson decays at 8 TeV [8, 9] and 13 TeV [10, 11]. As the angular correlations in term of the parameterization of Sec. II are skewed by the actual analyses, we briefly summarize the basic selection criteria for the different searches.

$4q$ Final State by ATLAS at 8 TeV

In the fully hadronic ATLAS search for diboson resonances at 8 TeV, jets are clustered with the C/A algorithm with radius $R = 1.2$, and events must have two jets with $p_T > 20$ GeV and $|\eta| < 2.0$. If there are electrons with $E_T > 20$ GeV and $|\eta| < 1.37$ or $1.52 < |\eta| < 2.47$, or if there are muons with $p_T > 20$ GeV and $|\eta| < 2.5$, the event is vetoed. Events must also have $\not{E}_T < 350$ GeV.

The two fat jets are then filtered with $y_{\min} = 0.04$. The constituents of the two subjets of the groomed jet are then reclustered again with the C/A algorithm but with a smaller cone size of $R = 0.3$. The up to three highest-p_T jets, which we will call *filtered jets*, are used to reconstruct the W or Z boson candidate. Having reconstructed the ungroomed, groomed, and filtered jets, further event selection cuts are applied. The rapidity difference between the ungroomed jets must satisfy $|y_{J_1} - y_{J_2}| < 1.2$. Additionally, the p_T asymmetry of ungroomed jets must be small, $(p_{T,\,J_1} - p_{T,\,J_2}) \,/\, (p_{T,\,J_1} + p_{T,\,J_2}) < 0.15$. The ungroomed and corresponding groomed and filtered jets are tagged as a W or Z boson if they fulfill the following three criteria:

- The pair of subjets of the groomed jet must satisfy a stronger transverse momentum balance requirement, $y \geq y_{\min} = 0.2025$.

- The number of charged tracks associated to the ungroomed jet has to be less than $n_{\rm trk} < 30$. Only well-reconstructed tracks with $p_T \geq 500$ MeV are used.

- The W or Z boson candidates, reconstructed from the filtered jets, are finally tagged as a W and/or Z, if their invariant mass fulfills $|m_J - m_V| < 13$ GeV. Here, m_V is either 82.4 GeV for a W boson or 92.8 GeV for a Z boson, as determined ATLAS full simulation.

Finally, the event is required to have the two highest-p_T jets be boson-tagged and $m_{JJ} > 1.05$ TeV.

$4q$ Final State by CMS at 8 TeV

The CMS 8 TeV analysis uses jet pruning to reconstruct a diboson resonance. Jets are reconstructed with the C/A algorithm using $R = 0.8$, and events must have at least two jets with $p_T > 30$ GeV and $|\eta| < 2.5$, where the two leading jets must satisfy $|\Delta\eta| < 1.3$ and $m_{JJ} > 890$ GeV. The two jets are pruned with $z_{\min} = 0.1$ (roughly equivalent to $y_{\min} = 0.11$) and the corresponding W/Z candidate must satisfy 70 GeV $< m_J <$ 100 GeV. Jets are further categorized according to their purity using the N-subjettiness ratio τ_{21}, where high-purity W/Z candidates have $\tau_{21} < 0.5$ and low-purity W/Z candidates have $0.5 < \tau_{21} < 0.75$. The diboson resonance search requires at least one high-purity W/Z jet, and the second W/Z can be either high- or low-purity.

$4q$ Final State by ATLAS at 13 TeV

In ATLAS 13 TeV analysis, events are again vetoed if they contain electrons or muons with $p_T > 25$ GeV and $|\eta| < 2.5$, and events must have $\not{E}_T < 250$ GeV. In contrast to earlier, though, jets are now clustered using the anti-k_T cluster algorithm [124] with $R = 1.0$, and events must have two fat jets with $p_T > 200$ GeV, $|\eta| < 2.0$ and $m_J > 50$ GeV. The leading jet must have $p_T > 450$ GeV, the invariant mass of the two fat jets must lie between 1 TeV and 2.5 TeV, and the rapidity separation must be small, $|y_{J_1} - y_{J_2}| < 1.2$. Furthermore, the leading two jets must also have a small p_T asymmetry, $(p_{T,\ J_1} - p_{T,\ J_2}) \,/\, (p_{T,\ J_1} + p_{T,\ J_2}) < 0.15$.

Jets are then trimmed, instead of filtered, by reclustering with the k_T algorithm using $R = 0.2$ and using hardness parameter $z_{\min} = 0.05$, and the energy correlation functions for $D_2^{(\beta=1)}$ are then calculated on the trimmed jets to help distinguish W bosons, Z bosons, and multijet background. The upper limit on D_2 varies for W and Z candidates as well as the p_T of the trimmed jet: to implement this D_2 cut, we linearly interpolate between the two cut values, $D_2 = 1.0$ at $p_T = 250$ GeV and $D_2 = 1.8$ at $p_T = 1500$ GeV, quoted in their analysis. The trimmed jets are tagged as bosons if they fulfill two final criteria: $N_{\text{trk}} < 30$ for charged-particle tracks associated with the ungroomed jet and $|m_J - m_V| < 15$ GeV, where $m_V = 84$ GeV for a W boson and $m_V = 96$ GeV for a Z boson.

$4q$ Final State by CMS at 13 TeV

The CMS 13 TeV analysis shares many of the same selection criteria as their 8 TeV analysis, with the following adjustments. The two anti-k_T, $R = 0.8$, $p_T > 30$ GeV jets must now lie within $|\eta| < 2.4$. The pseudorapidity separation between the two jets must again satisfy $|\Delta\eta| < 1.3$, and the minimum invariant mass cut on m_{JJ} is raised to 1 TeV. The two jets are again pruned with $z_{\min} = 0.1$ and the pruned jet mass window is widened, allowing 65 GeV$< m_{W/Z} <$ 105 GeV.

Finally, the N-subjettiness ratio τ_{21} is again calculated, where high-purity W/Z jets must have a slightly harder requirement, $\tau_{21} \leq 0.45$, and low-purity W/Z jets satisfy $0.45 < \tau_{21} < 0.75$. The event must have at least one high-purity W/Z jet and is classified as high-purity or low-purity according to the second jet.

C. Analysis effects and reconstruction

We implement the fully hadronic ATLAS and CMS diboson searches on the signal samples presented in Sec. III A, and we extract the angular observables reviewed in Sec. II A from the subjets of the reconstructed W/Z-tagged boson. Since W/Z discrimination is very difficult in this final state, we merge the $\cos\theta_{p_1}$ and $\cos\theta_{p_3}$ distributions into a single differential distribution labeled $\cos\theta_q$ and do not differentiate between W and Z candidates. We also recognize that these analyses do not attempt to distinguish quarks from anti-quarks, hence we randomly assign the p_1 and p_2 labels (or p_3 and p_4 labels) to subjets of a given W/Z candidate, which renders the signs of different angles ambiguous. Finally, we merge the high-purity and low-purity tagged events in the CMS analyses to ensure our angular sensitivity analysis has reasonable statistics.

We find that of the angles defined in Sec. II, the main discrimination power between different spin scearios comes from $\cos\theta^*$, $\cos\theta_q$ and Ψ. In the remainder of this Section, we will present the individual differential shapes for the different Monte Carlo samples and experimental studies, and explain how they are skewed by the respective event selection and jet substructure cuts. All of our figures show both parton and reconstruction level unit-normalized distributions for the different signal samples and QCD multijet background, where all showering, hadronization, detector resolution, jet reconstruction, and substructure analysis effects have been included in the reconstructed differential distributions.

Differential Shape of $\cos\theta^*$

We first show the angular observable $\cos\theta^*$ in Fig. 2 for various spin-0, spin-1, and spin-2 signal benchmarks and the QCD background after implementing the ATLAS 8 TeV (upper left), CMS 8 TeV (upper right), ATLAS 13 TeV (lower left), and CMS 13 TeV (lower right) analyses. This angle measures the alignment of the vector bosons from X decay with the beam axis, if we use the threshold approximation to identify the X rest frame with the lab frame. We see significant discrimination power at parton level (thin lines) between the different signal benchmarks, especially between the spin-0 and spin-2 signals compared to the spin-1 benchmark. The extra oscillations in

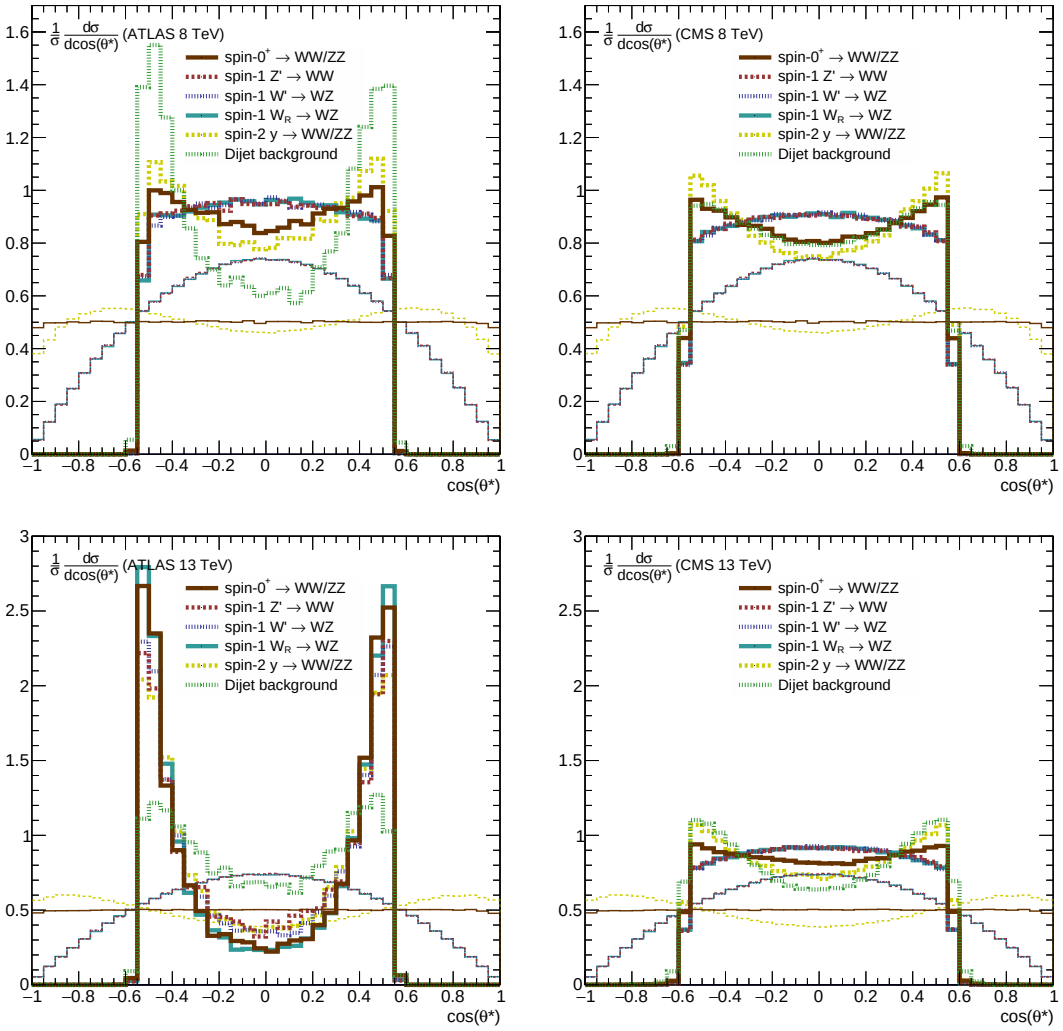

FIG. 2. Comparison of the $\cos\theta^*$ angle between MC parton level results (thin lines) and reconstruction of showered events via jet substructure (thick lines) for the ATLAS (left) and CMS (right) hadronic diboson search at 8 TeV (top) and 13 TeV (bottom). Each distribution is unit-normalized.

the spin-2 signal, however, are lost when comparing the reconstruction level (thick lines) distributions, leaving only the overal concavity of the spin-1 distribution the main discriminant from the spin-0, spin-2, and QCD background shapes. Comparing parton level to reconstruction level results for each signal sample, we see the experimental analyses cause significant hard cuts in $\cos\theta^*$, effectively requiring $|\cos\theta^*| \lesssim 0.55$ for ATLAS and $|\cos\theta^*| \lesssim 0.6$ for CMS, and we also see a deficit of events around $\cos\theta^* \approx 0$ is induced by each analysis, most notably in the ATLAS 13 TeV analysis.

We can identify the sharp cliffs in the $|\cos\theta^*|$ distribution with the cut on the maximum

pseudorapidity difference $|\Delta\eta|$ between the two fat jets, since the θ^* angle is directly related to the pseudorapidity via $\eta = -\log\tan(\theta/2)$. Therefore $\cos\theta^*$ can be rewritten in the X rest frame as

$$|\cos\theta^*| = \cos\left(2\arctan e^{-\frac{|\Delta\eta|}{2}}\right) = \tanh\frac{|\Delta\eta|}{2} \leq \tanh\frac{|\Delta\eta_{\max}|}{2} \ . \tag{14}$$

Given $|\Delta y_{\max}| = 1.2$ at ATLAS and $|\Delta\eta_{\max}| = 1.3$ at CMS, and since differences in pseudorapidity are invariant under longitudinal boosts, we therefore expect sharp cuts at $|\cos\theta^*| \approx 0.54$ and 0.57, respectively, where the steepness of the cliff is only spoiled by the net transverse momentum of the X resonance in the lab frame.

The deficit of events around $\cos\theta^* \approx 0$ is a direct result of the angular scale chosen for the jet substructure analysis, where a larger angular scale causes a stronger sculpting behavior around $\cos\theta^* \approx 0$. We know from Eq. 14 that small $\cos\theta^*$ is identified with small $\Delta\eta$ between the two fat jets, and we also show in Fig. 3 the parton level correlation between $\Delta\eta$ for the two fat jets and ΔR of the resulting W and Z decay products for a spin-1 W' example. Other signal samples would show a similar correlation, albeit with only one W (left color band) or Z (right color band) as appropriate. The bulk of the W/Z subjets lie at $\Delta R \approx 2m_{W/Z}/(1\text{ TeV})$ as expected, where 1 TeV is a rough estimate of the W and Z transverse momenta when the vector bosons are central, but we also see a clear correlation between larger $\Delta\eta$ separation between the fat jets and the corresponding ΔR of the resulting subjets. As $\Delta\eta$ grows, the vector bosons from the W' decay become more forward, and thus the corresponding p_T of each vector boson decreases, leading to larger ΔR separation of their subjets.

As a result of this correlation, using a large fixed angular scale during jet substructure reclustering leads to a deficit of events with small $\Delta\eta$ separation between fat jets and hence leads to the sculpting effect around $\cos\theta^* \approx 0$ observed in Fig. 2. A relatively large angular scale for subjet clustering will merge nearby partons together, and the resulting event will not have the requisite subjets to define the $\cos\theta^*$ angle and fail the reconstruction of angular observables. The ATLAS 13 TeV analysis has the most pronounced deficit of events around $\cos\theta^* \approx 0$, since this analysis uses a fixed radius of $R = 0.2$ during trimming. Most notably, using an angular scale of $R = 0.2$ during subjet clustering causes most of the quarks to merge into a single subjet, which severely limits the viability of such a subjet identification technique for a post-discovery study of angular correlations. We remark that the $D_2^{(\beta=1)}$ discriminant also used in the ATLAS 13 TeV analysis to identify a prevalence of two-prong energy correlations compared to one-prong and three-prong energy correlations fails to ameliorate the situation, as the events with the strongest two-prong behavior would still need to be reclustered to identify the appropriate subjets for angular observable studies.

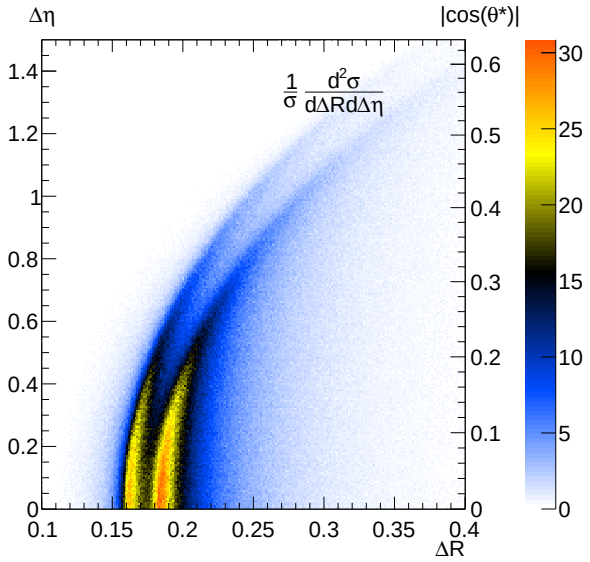

FIG. 3. Spin-1 W' parton level correlation of the angular separation ΔR between the W/Z decay products and the rapidity difference $\Delta\eta$ of the two $W' \to WZ$ fat jets, where the left band shows the W decay products and the right band shows the Z decay products, and the shading shows the relative event weight. This correlation holds also for other spin scenarios. The $\Delta\eta$ axis is translated to a $|\cos\theta^*|$ axis according to Eq. 14.

Differential Shape of $\cos\theta_q$

The second main discriminant between different spin signal hypotheses is the $\cos\theta_q$ angle, shown in Fig. 4, which combines the $\cos\theta_{p_1}$ and $\cos\theta_{p_3}$ angles defined in Sec. II. This angle measures the alignment of the outgoing quark with the boost vector of its parent vector in the parent rest frame, and since each event has two vector candidates, each event contribues twice to the distribution. Again we first focus on the parton level results (thin lines), which show that the spin-2 RS graviton hypothesis has the opposite concavity to the spin-0 and spin-1 signals. We note that the spin-2 resonance dominantly couples to tranversely polarized electroweak bosons, while the spin-0 and spin-1 resonances dominantly couple to longitudinal bosons. Hence, the pronounced difference in shape between the signals is a realistic proxy for studying the sensitivity of different jet substructure analyses to the polarization of W and Z bosons. For longitudinal bosons, the expected analytic shape of the $\cos\theta_q$ distribution is $\frac{3}{4}\left(1-\cos^2\theta_q\right)$, while the shape is $\frac{3}{8}\left(1+\cos^2\theta_q\right)$ for transverse bosons [101]. We remark that enhancing sensitivity to either the center or edges of the $\cos\theta_q$ distribution will emphasize sensitivity to longitudinal or transverse gauge bosons, respectively.

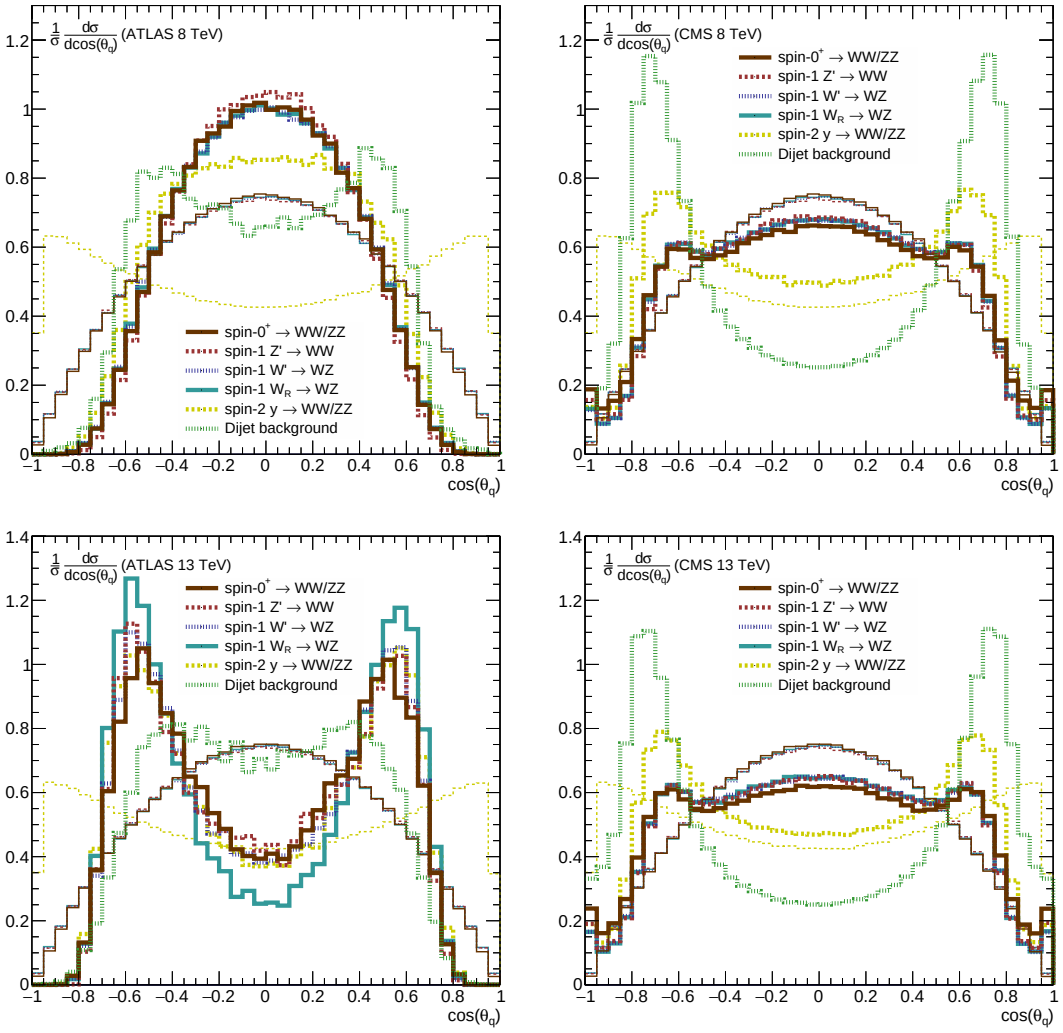

FIG. 4. Comparison of the $\cos\theta_q$ angle between MC parton level results (thin lines) and reconstruction of showered events via jet substructure (thick lines) for the ATLAS (left) and CMS (right) hadronic diboson search at 8 TeV (top) and 13 TeV (bottom).

These results also agree with an earlier analysis by CMS [125], but we carry the analysis further by studying multiple state-of-the-art jet substructure techniques to understand the impact of vector boson polarization on the resulting reconstruction efficiency.

Turning to the reconstructed angular distributions (thick lines) in Fig. 4, we again see the full phase space of the parton decays gets significantly molded by the experimental analyses, where events close to $\cos\theta_q \approx \pm 1$ are cut away. In contrast to the sharp cliffs in $\cos\theta^*$, though, the $\cos\theta_q$ distribution exhibits a milder transformation, and start and strength of the deviations depend strongly on the individual analysis. At 8 TeV, ATLAS shows a reversal point at $\cos\theta_q \approx \pm 0.6$,

whereas the CMS reversal point is $\cos\theta_q \approx \pm 0.8$. We also observe a deficit of events with $\cos\theta_q \approx 0$, most notably in the ATLAS 13 TeV analysis.

In order to understand the behavior around $\cos\theta_q \approx \pm 1$, we derive an approximate relation between $\cos\theta_q$ and the subjet p_T ratio y. Identifying $\cos\theta_q$ with $\cos\theta_{p_1}$ for the moment, we write $\cos\theta_q \equiv \hat{p}_{p_1} \cdot \hat{p}_{V_2}$ from Eq. 1, where the p_1 and V_2 four-momenta are boosted to the V_1 rest frame. If we assume threshold production of X, then the X rest frame is identified with the lab frame, and the two vectors V_1 and V_2 are completely back-to-back in both frames. Hence, $\hat{p}_{V_2}$ in the V_1 rest frame can be replaced by the (negative) boost direction $-\hat{p}_{V_1}$ going from the lab frame to the V_1 rest frame. If we now take the limiting case that V_1 and V_2 have no longitudinal momentum, then we are left with six four-momentum components of p_1 and p_2, which are the decay products of V_1, subject to four constraints: $(p_1 + p_2)^2 = m_{V_1}^2$, $p_1^2 = p_2^2 = 0$, and $y = p_{T_2}/p_{T_1}$ given by the $y_{\min}$ cut parameter. We choose the two remaining free parameters to be the transverse momentum of the boson, $p_{T,\,V_1}$ and the angle between the decay plane spanned by p_1 and p_2 relative to the transverse plane. We have three planes: the plane spanned by the beam axis and the V_1 boson, the transverse plane, and the decay plane spanned by p_1 and p_2, where the common axis of intersection is the V_1 transverse momentum vector.

For the limiting case that the decay plane spanned by p_1 and p_2 aligns with the transverse plane, the cut on y provides a lower bound on $|\cos\theta_q|$, while the case when the decay plane aligns with the plane spanned by the beam axis and the V_1 boson provides an upper bound on $|\cos\theta_q|$, where we can only bound $|\cos\theta_q|$ because we order the two subjets in p_T. These lower and upper limits are[1]

$$\frac{p_{T,\,V}}{\sqrt{m_V^2 + p_{T,\,V}^2}} \frac{1-y}{1+y} \leq |\cos\theta_q| \leq \frac{\sqrt{m_V^2 + p_{T,\,V}^2}}{p_{T,\,V}} \frac{1-y}{1+y} \,. \tag{15}$$

Note that the upper bound can in principle exceed 1, and at this point, for a given $p_{T,\,V}$ and y, the solution with the decay plane aligned with the beam axis becomes unphysical and a rotation of the decay plane away from the beam axis is needed to obtain a physical solution. If we relax the initial conditions and allow longitudinal boosts of the system, the resulting y cut will, by construction, project out only the transverse components of the boost needed to transform the lab frame into the rest frame of V_1. This smears the expression in Eq. 15 for both the upper and lower limits.

[1] It is easiest to derive these limits by performing an azimuthal rotation of the system to fix the V_1 transverse momentum in the $\hat{y}$ direction.

Nevertheless, we can see that in the limit $p_{T,\,V} \gg m_V$,

$$|\cos\theta_q| \approx \frac{1-y}{1+y} \leq \frac{1-y_{\min}}{1+y_{\min}} \ . \tag{16}$$

For $y_{\min} = 0.20$, 0.11, or 0.05 for the ATLAS 8 TeV, CMS, and ATLAS 13 TeV analyses, respectively, we expect edges in the $|\cos\theta_q|$ distribution at approximately 0.66, 0.80, and 0.90. As mentioned before, the analytic calculation above requires assumptions about the necessary boost to move from the lab frame to the V_1 rest frame and taking $p_{T,\,V} \gg m_V$, and if these assumptions are violated, the upper limit on $|\cos\theta_q|$ can be exceeded.

This discussion explains the results in Fig. 4, except for the ATLAS 13 TeV analysis, where many more events are lost then simply those beyond the derived edge at $|\cos\theta_q| = 0.9$. This is because the ATLAS 13 TeV imposes an effectively tighter $y_{\min}$ criteria via the $D_2^{(\beta=1)}$ discriminant, which we demonstrate in Fig. 5. We see that an event with a low subjet p_T ratio would generally have a large value of $D_2^{(\beta=1)}$ and thus be removed given the D_2 cut. As a reminder, the D_2 cut parameter varies from $D_2 = 1.0$ for a trimmed jet of $p_T = 250$ GeV to $D_2 = 1.8$ for $p_T = 1500$ GeV, which corresponds to $y_{\min} \approx 0.1$–0.2, in agreement with the resulting sculpting seen in Fig. 4.

Finally, the deficit of events with $\cos\theta_q \approx 0$ is the same sculpting effect as seen before around $\cos\theta^* \approx 0$. In Fig. 6, we show the correlation between ΔR of the W/Z decays and the ratio of quark transverse momentum y for parton-level $W' \to WZ$ events. As before, the left band shows the $W^\pm$ daughter partons and the right band shows the Z daughter quarks. Since using a large ΔR during subjet finding causes the W/Z decay partons to be merged, events with large y are more likely to be removed from the event sample by subsequent kinematic cuts. Using Eq. 16, we can relate y to an effective cut on $\cos\theta_q$, which explains the deficit of events seen around $\cos\theta_q \approx 0$ in Fig. 4, most notably in the lower left panel for the ATLAS 13 TeV analysis.

Differential Shape of Ψ

As shown in Fig. 7, the differential distribution in the angle Ψ is flat for all spin hypotheses except for the spin-2 resonance.[2] We will thus focus on explaining the behavior of the spin-2 scenario. In this distribution, we expect amplitudes proportional to 1 and $\cos(4\Psi)$, where the

[2] Recall $\Psi = \Phi_{V_1} + \Phi/2$ is the average azimuthal angle of the two decay planes formed by the vector boson decay products. Also, note that the lower left panel showing the ATLAS 13 TeV analysis is dominated by statistical fluctuations, which occurs because the $R = 0.2$ substructure angular scale has poor efficiency at finding four distinct subjets needed to reconstruct the two decay planes.

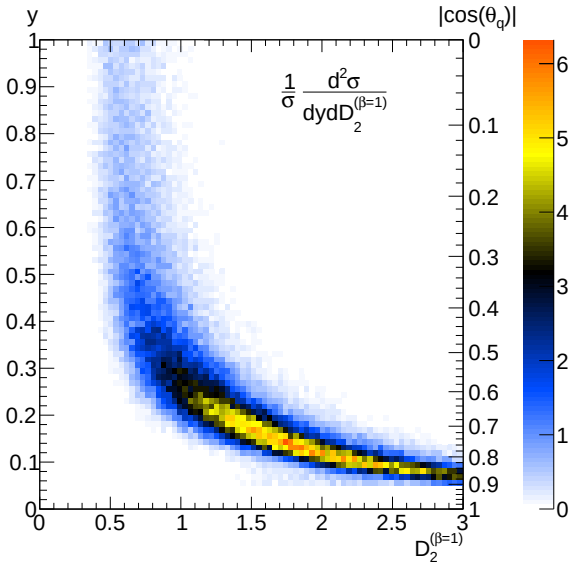

FIG. 5. Correlation between the energy correlation function $D_2^{(\beta=1)}$ and the ratio of transverse momentum y of the two leading subjets, where the shading shows the relative event weight. All analysis cuts of the ATLAS 13 TeV analysis are applied, except the cut on $D_2^{(\beta=1)}$ itself. This particular plot is based on the spin-1 W' model, but the correlation seen holds also for other spin scenarios. The y axis is translated to a $|\cos\theta_q|$ axis according to Eq. 16.

respective amplitudes at parton level depend on the helicity states of the vector bosons and the production level partons [100, 101]. A $\cos(2\Psi)$ contribution would only appear when particles and anti-particles of the V decay can be distinguished. Curiously, the differential distribution of Ψ after cuts causes the $\cos(4\Psi)$ amplitude to increase. This is related to the same two cuts on $\Delta\eta_{JJ,\,\mathrm{max}}$ and subjet p_T ratio y_{min}, which already skewed the $\cos\theta^*$ and $\cos\theta_q$ angle.

We can analytically determine the differential shape of the Ψ distribution as a function of the cut values on $\Delta\eta_{JJ,\,\mathrm{max}}$ and y_{min}, using the fully differential results in Ref. [101]. The normalized shape can be expressed as

$$\frac{1}{\sigma^{(\text{spin-2})}}\frac{d\sigma^{(\text{spin-2})}}{d\Psi} = \frac{1}{2\pi} - \mathcal{A}(y_{\mathrm{min}}, \Delta\eta_{\mathrm{max}})\cos(4\Psi)\ , \tag{17}$$

with

$$\begin{aligned}\mathcal{A} = \frac{1}{24\pi} F_{+-}\left(1+4y_{\mathrm{min}}+y_{\mathrm{min}}^2\right)^2(5f_{q\bar{q}}-1)(8+6\cosh\Delta\eta_{\mathrm{max}}+\cosh 2\Delta\eta_{\mathrm{max}})\Big/ \\ \Big[F_{+-}\left(1+y_{\mathrm{min}}+y_{\mathrm{min}}^2\right)^2\Big((5f_{q\bar{q}}+1)(1+2\cosh\Delta\eta_{\mathrm{max}})+2\cosh 2\Delta\eta_{\mathrm{max}}\Big)+ \\ F_{00}\left(1+4y_{\mathrm{min}}+y_{\mathrm{min}}^2\right)^2(-15f_{q\bar{q}}+8+6\cosh\Delta\eta_{\mathrm{max}}+\cosh 2\Delta\eta_{\mathrm{max}})\Big]\ .\end{aligned} \tag{18}$$

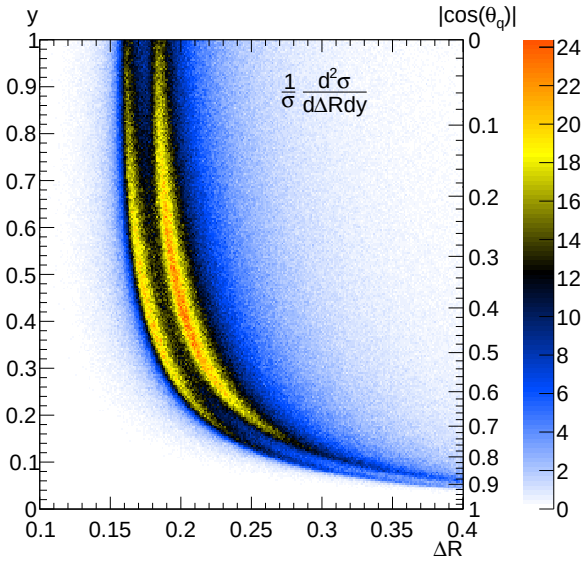

FIG. 6. Spin-1 W' parton level correlations of the angular separation ΔR between the W/Z decay products and their ratio in transverse momentum y, where the shading shows the relative event rate. This basic correlation holds also for other spin scenarios. The y axis is translated to an approximate $|\cos\theta_q|$ axis according to Eq. 16.

Here, $F_{\lambda_1\lambda_2}$ is the fraction of events with two gauge bosons having a helicity λ_1 and λ_2 respectively, and $f_{q\bar{q}}$ is the production fraction from $q\bar{q}$ initial state quarks. From our Monte Carlo simulation at 8 TeV, we find $F_{+-} = F_{-+} = 45.8\%$, $F_{00} = 7.8\%$ and 0.6% others, and thus we neglected the subleading helicity components, which are suppressed by powers of $m_{W/Z}/m_X$. Furthermore, we find $f_{q\bar{q}} \approx 65.5\%$ at 8 TeV LHC, while it drops to $f_{q\bar{q}} \approx 45.0\%$ at 13 TeV LHC. We show the scaling behaviour of $\mathcal{A}$ in Fig. 8.

From Fig. 8, we can directly read off the expected $\cos(4\Psi)$ amplitude for our 8 TeV and 13 TeV signal sample. Using $y_{\min} \to 0$ and $\Delta\eta_{JJ,\,\max} \to \infty$ the predicted amplitudes at parton level match with $\mathcal{A} \approx 0.014$ at 8 TeV and $\mathcal{A} \approx 0.0077$ at 13 TeV very well our Monte Carlo simulation. Including cuts we expect $\mathcal{A} \approx 0.045$ and $\mathcal{A} \approx 0.034$ for ATLAS and CMS at 8 TeV, respectively, and $\mathcal{A} \approx 0.021$ for CMS at 13 TeV. For CMS the expected amplitude is slightly larger than that seen in Fig. 7, which can be explained by the approximation of Eq. 16 used to relate $\cos\theta_q$ with $y_{\min}$.

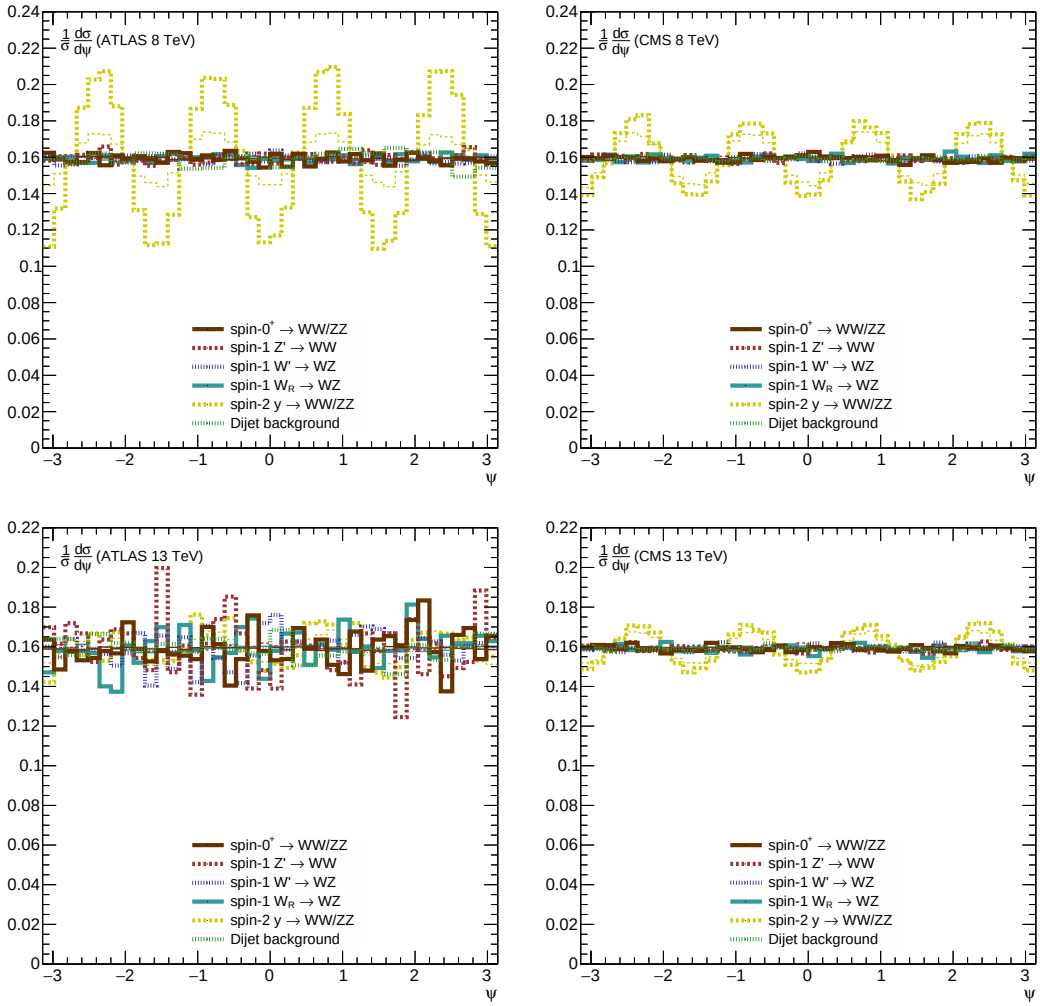

FIG. 7. Comparison of the Ψ angle between MC parton level results (thin lines) and reconstruction of showered events via jet substructure (thick lines) for the ATLAS (left) and CMS (right) hadronic diboson search at 8 TeV (top) and 13 TeV (bottom).

IV. ANGULAR OBSERVABLES IN SEMI-LEPTONIC FINAL STATES

We now turn to the semi-leptonic analyses, $X \to \ell\ell qq$ and $X \to \ell\nu qq$, which provide important cross-channels for a future discovery of a diboson resonance. To reiterate, the relative rates of the $4q$, $\ell\ell qq$, and $\ell\nu qq$ final states will disentangle the intermediate W^+W^-, $W^\pm Z$, and ZZ nature of the resonance, which is very difficult to do using only the $4q$ analysis. Moreover, the semileptonic channels enjoy cleaner reconstruction of angular observables, larger signal efficiencies, and better control of systematic uncertainties, counterbalanced by lower overall statistical power. The importance of the semileptonic channel, especially compared to the fully leptonic channel, was

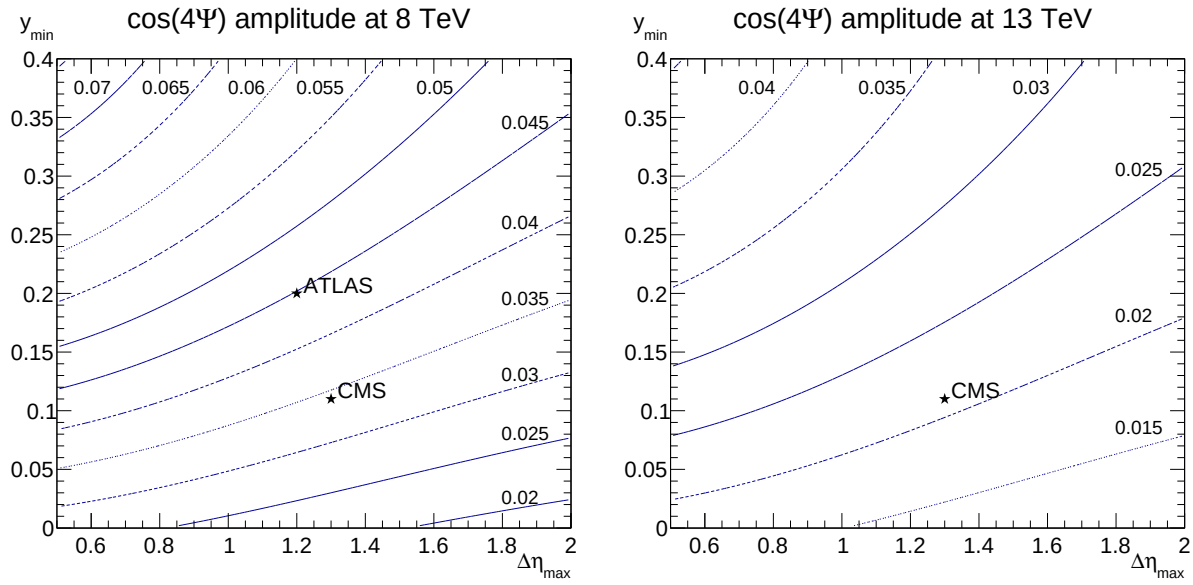

FIG. 8. Expected cos(4Ψ) amplitude $\mathcal{A}$ (contours) for a spin-2 resonance at 8 TeV (left) and 13 TeV (right) as function of the cut parameter $y_{\min}$ and $\Delta\eta_{JJ,\,\max}$, as shown in Eq. 18. We use $F_{+-} = F_{-+} = 45.8\%$ and $F_{00} = 7.8\%$, as determined from our underlying Monte Carlo simulation, and $f_{q\bar{q}} = 65.5\%$ and $f_{q\bar{q}} = 45.0\%$ for 8 TeV and 13 TeV, respectively. We also show the respective working points of ATLAS and CMS, except for ATLAS at 13 TeV, where the effective $y_{\min}$ is not a fixed parameter.

emphasized, for example, in Refs. [126, 127]. In particular, the angular observables $\cos\theta_{p_1}$ and $\cos\theta_{p_3}$, which were previously combined into $\cos\theta_q$ because we could not trace a given parent from one event to the next, are now assigned as $\cos\theta_q$ and $\cos\theta_l$. In addition, for the $\ell\nu qq$ analysis, the $\cos\theta_l$ distribution is asymmetric because the charge of the lepton distinguishes leptons from the anti-lepton, in constrast to the $4q$ case. We begin again by summarizing the semi-leptonic analyses by ATLAS and CMS [11, 13, 14, 17, 19, 20] and then present the corresponding angular distributions.

A. ATLAS and CMS semi-leptonic analyses at 8 TeV and 13 TeV

$\ell\ell qq$ Final State by ATLAS at 8 TeV

In the $\ell\ell qq$ ATLAS analysis at 8 TeV, events are required to have exactly two muons of opposite charge or two electrons, where muons must have $p_T > 25$ GeV and $|\eta| < 2.4$ and electrons must have $p_T > 25$ GeV and $|\eta| < 2.47$, excluding $1.37 < |\eta| < 1.52$. In addition, all leptons must pass a track isolation (calorimeter isolation) requirement (see Ref. [13] for details). The lepton pair must have 66 GeV$< m_{\ell\ell} <$ 116 GeV and $p_T^{\ell\ell} > 400$ GeV.

Jets are clustered using the C/A algorithm with $R = 1.2$ and need to have $p_T > 100$ GeV and $|\eta| < 1.2$. One jet needs to survive the grooming procedure with $y_{\min} = 0.2025$ and fulfill $p_T > 400$ GeV and 70 GeV$< m <$110 GeV.

$\ell\ell qq$ Final State by CMS at 8 TeV

In the CMS 8 TeV $\ell\ell qq$ analysis, electrons with $p_T > 40$ GeV and $|\eta| < 2.5$, excluding $1.44 < |\eta| < 1.56$, muons with $p_T > 20$ GeV and $|\eta| < 2.1$ are selected, and all leptons must be isolated from other tracks as well as in the calorimeter. Two same flavor, opposite charge, leptons are required, and for dimuon events, the leading muon must have $p_T > 40$ GeV. The lepton pair must have 70 GeV $< m_{\ell\ell} <$ 110 GeV.

Jets are reconstructed with the C/A algorithm using $R = 0.8$ and must have $p_T > 30$ GeV and $|\eta| < 2.4$. They are pruned with $z_{\min} = 0.1$ and are categorized by purity according the N-subjettiness variable τ_{21}, analogous to the CMS $4q$ search. The pruned jet mass must lie within 65 GeV $< m_J <$ 110 GeV. Both the leptonic and hadronic vector boson candidates must have $p_T^V > 80$ GeV and satisfy $m_{VV} > 500$ GeV. If there are multiple hadronic V candidates, the hardest p_T candidate in the higher purity category is used.

$\ell\ell qq$ Final State by ATLAS at 13 TeV

ATLAS uses the same kinematic acceptance cuts on electrons and muons in the 13 TeV analysis as the 8 TeV analysis, and track isolation requirements are imposed. Two muons of opposite charge or two electrons are required, where the lepton pair must have 66 GeV $< m_{\mu^+\mu^-} <$ 116 GeV or 83 GeV$< m_{e^+e^-} <$ 99 GeV, respectively.

Jets are clustered using the anti-k_T algorithm with $R = 1.0$ and are required to have $p_T > 200$ GeV and $|\eta| < 2.0$. The leading jet must satisfy the trimming procedure with $z_{\min} = 0.05$, and fulfill $p_T^J > 0.4 m_{\ell\ell J}$ and 68.2 GeV $< m_J <$ 108.4 GeV. Additionally, the jet needs to statisfy an upper bound on the $D_2^{(\beta=1)}$ energy correlator function. For simplicity, we linearly interpolate the D_2 cut between the two points quoted, $D_2 < 1.0$ at $p_T^J = 250$ GeV and $D_2 < 1.8$ at $p_T^J = 1500$ GeV. Finally, the dilepton system must have $p_T^{\ell\ell} > 0.4 m_{\ell\ell J}$.

$\ell\nu qq$ Final State by ATLAS at 8 TeV

In the 8 TeV ATLAS $\ell\nu qq$ analsis, the lepton kinematic criteria are the same as their 8 TeV $\ell\ell qq$ search, and a similar isolation criteria is used. Missing transverse energy $\not{E}_T$ (MET) must exceed 30 GeV and is used to calculate the corresponding neutrino four-momentum assuming no other

source of MET and $m_W^2 = (p_\ell + p_\nu)^2$:

$$p_z^\nu = \frac{1}{2p_T^\ell}\left[(m_W^2 + 2\vec{p}_T^{\,\ell}\cdot\vec{p}_T^{\,\nu})p_z^{\,\ell} \pm E^\ell\sqrt{(m_W^2 + 2\vec{p}_T^{\,\ell}\cdot\vec{\not{E}}_T)^2 - 4(p_T^\ell)^2\not{E}_T^2}\right] . \tag{19}$$

In the case of two complex solutions for p_Z^ν, the real part is used, otherwise the smaller solution in absolute value is used. Events are required to have $p_T^{\ell\nu} > 400$ GeV.

Jets are clustered using the C/A algorithm with $R = 1.2$. One jet must survive the grooming procedure with $y_{\min} = 0.2025$ and fulfill $p_T^J > 400$ GeV, $|\eta| < 2.0$ and 65 GeV $< m_J <$ 105 GeV, and the $\Delta\phi$ between this jet and the MET vector must exceed 1. Events with at least one b-tagged jet are vetoed (see Ref. [14] for details).

$\ell\nu qq$ Final State by CMS at 8 TeV

At CMS, electrons with $p_T > 90$ GeV and $|\eta| < 2.5$, excluding $1.44 < |\eta| < 1.56$, and muons with $p_T > 50$ GeV and $|\eta| < 2.1$ are selected. The same isolation criteria from the CMS $\ell\ell qq$ search are applied. A single muon or electron is required and MET must exceed 40 GeV or 80 GeV, respectively. The corresponding neutrino four-momentum is reconstructed as in the ATLAS $\ell\nu qq$ search, and $p_T^{\ell\nu} > 200$ GeV is required.

Jets are reconstructed with the C/A algorithm using $R = 0.8$, $p_T > 30$ and $|\eta| < 2.4$. They are pruned with $z_{\min} = 0.1$ and categorized by purity using τ_{21}, as in the CMS $4q$ and $\ell\ell qq$ searches. The pruned jet mass must again lie within 65 GeV $< m_J <$ 110 GeV and have $p_T^J > 200$ GeV, and if there are multiple hadronic V candidates, the hardest p_T candidate in the higher purity category is used. Furthermore, $\Delta R_{J,\,(\ell\nu)} > \pi/2$, $\Delta\phi_{J,\,\not{E}_T} > 2.0$, $\Delta\phi_{J,\,(\ell\nu)} > 2.0$ and $m_{J\ell\nu} > 700$ GeV are required. Events with one b-tagged jet are vetoed.

$\ell\nu qq$ Final State by ATLAS at 13 TeV

For the ATLAS 13 TeV $\ell\nu qq$ search, leptons are identified as in the ATLAS $\ell\ell qq$ final state search at 8 TeV. Events must have one lepton and $\not{E}_T > 100$ GeV, and the neutrino four-momentum is reconstructed as in the 8 TeV analysis.

Jets are clustered using the anti-k_T algorithm with $R = 1.0$. The leading jet must survive the trimming procedure with $z_{\min} = 0.05$ and fulfill $p_T > 200$ GeV, $|\eta| < 2.0$, 70.2 GeV $< m_J <$ 106.4 GeV, and $p_T^J > 0.4 m_{\ell\nu J}$. The same $D_2^{(\beta=1)}$ energy correlator cut as the 13 TeV $\ell\ell qq$ ATLAS search is imposed. Finally, events must have $p_T^{\ell\nu} > 0.4 m_{\ell\nu J}$ and $p_T^{\ell\nu} > 200$ GeV, and events with b-tagged jets are vetoed.

$\ell\nu qq$ Final State by CMS at 13 TeV

Lastly, for the CMS $\ell\nu qq$ search at 13 TeV, events must have a single electron or muon, where electron candidates must have $p_T > 120$ GeV and $|\eta| < 2.5$, excluding $1.44 < |\eta| < 1.56$, and muon candidates must have $p_T > 53$ GeV and $|\eta| < 2.1$. The same lepton isolation criteria as the CMS $\ell\ell qq$ search are applied. Electron (muon) events must have at least 80 GeV (40 GeV) of MET. The neutrino four-momentum is reconstructed as in the ATLAS $\ell\nu qq$ final state search, and the lepton-neutrino system must have $p_T^{\ell\nu} > 200$ GeV.

Jets are reconstructed with the anti-k_T algorithm using $R = 0.8$, $p_T > 30$ GeV and $|\eta| < 2.4$. They are pruned with $z_{\rm min} = 0.1$ and categorized by purity using the same criteria as the 13 TeV CMS $4q$ search. To satisfy the boson tagging requirements, a pruned jet J has to fulfill 65 GeV $< m_J <$ 105 GeV and $p_T^J > 200$ GeV, and for events with multiple hadronic boson candidates, the highest p_T jet with the higher purity category is used. Events must also pass $\Delta R_{J,\,(\ell\nu)} > \pi/2$, $\Delta\phi_{J,\,\not{E}_T} > 2.0$, $\Delta\phi_{J,\,(\ell\nu)} > 2.0$, and $m_{J\ell\nu} > 700$ GeV cuts, and events with b-tagged jets are vetoed.

B. Angular observables in semi-leptonic final states and comparison with fully hadronic final states

In Fig. 9, we show the normalized distributions for the $\cos\theta^*$, $\cos\theta_q$, $\cos\theta_l$, and Ψ angles for the relevant ATLAS and CMS $\ell\ell qq$ analyses. Note that we do not show the $\ell\ell qq$ background or the parton-level results in this plots. The $\ell\ell qq$ final state mimics the $4q$ final state, since the entire $X \to \ell\ell qq$ system is in principle reconstructible. Moreover, as mentioned before, the $\cos\theta_q$ distribution for the $4q$ final state splits into the new $\cos\theta_q$ and $\cos\theta_l$ angles, because the final state partons are distinguishable. On the other hand, the $\ell\ell qq$ final state pays an intrinsic penalty in statistical power, since the branching ratio $\mathrm{Br}(W^\pm Z \to \ell\ell qq)$ / $\mathrm{Br}(W^\pm Z \to 4q) \approx 0.094$, for $\ell = e,\, \mu$, is only partially mitigated by an improved semileptonic signal efficiency. Thus, the $4q$ and semileptonic channels play important complementary roles both in the discovery of a new resonance but also give significant cross-checks for spin discrimination.

From Fig. 9, we see that angular observables again provide important discrimination power between spin-2 and the other spin hypotheses, while the main sensitivity to distinguish spin-0 from spin-1 resonances comes from the $\cos\theta^*$ angle. The sculpting effects we identified earlier are still evident in $\cos\theta_q$ as a result of the jet substructure cuts, but on the other hand, most of the phase

space is preserved for the $\cos\theta_l$ distribution. Note that there is no p_T requirement on the individual subjets in contrast to the hard cut on the lepton p_T. This effectively flattens the $\cos\theta_l$ shape for the spin-2 resonance compared to $\cos\theta_q$, as events with large lepton p_T imbalance near $\cos\theta_l = \pm 1$ tends to miss one of the leptons.

One interesting feature is the sharp cliff in $\cos\theta^*$ for the ATLAS 13 TeV analysis, shown in the top row, rightmost panel of Fig. 9. This is directly connected to the $p_T^{\ell\ell} > 0.4 m_{\ell\ell J}$ and $p_T^J > 0.4 m_{\ell\ell J}$ cuts, because from Eq. 4, we see that the corresponding maximum pseudorapidity gap between the vector boson candidates is $\Delta\eta_{\rm max} \sim 2.1$, which leads to a maximum of $|\cos\theta^*| = 0.6$. We also note the ATLAS 8 TeV analysis has cliffs at $|\cos(\theta^*)| \lesssim 0.92$ in the ATLAS 8 TeV analysis, driven by their milder cuts on $p_T^{\ell\ell} > 400$ GeV and $p_T^J > 400$ GeV.

In this regard, the most discrimination power between the various spin scenarios follows from the CMS 8 TeV analysis, where the spin-0 and spin-2 curves are readily distinguished from the spin-1 shapes. In contrast, the ATLAS 13 TeV analysis molds the $\cos\theta^*$ distribution to eliminate any possibility of distinguishing these different spins.

In Fig. 10, we show the normalized distributions for $\cos\theta^*$, $\cos\theta_q$, and $\cos\theta_l$ for the ATLAS and CMS 8 TeV and 13 TeV analyses. We remark that Ψ has no discriminating power between the signal hypotheses, so we omit it from the figure. The $\cos\theta_q$ distributions are similar to those from before, while the $\cos\theta_l$ shows a novel asymmetry.

The asymmetries in the $\cos\theta_l$ distributions are the result of contamination by leptonic τ decays. In particular, the extra neutrinos from the $\tau \to e\nu\nu$ and $\tau \to \mu\nu\nu$ decays skew the reconstruction of the leptonic decay of the $W^\pm$, where the additional neutrinos result in a false reconstruction of the rest frame of the $W^\pm$. This incorrect rest frame preferentially groups the charged lepton used for the $\cos(\theta_l)$ calculation closer to the boost vector needed to move to the $W^\pm$ rest frame, skewing the $\cos\theta_l$ distribution toward the $+1$ edge.

We also note, analogous to the $\ell\ell qq$ final state, the clear cliffs in the $\cos\theta^*$ distribution evident in the ATLAS 13 TeV analysis. These cliffs again arise from the $p_T^{\ell\nu} > 0.4 m_{\ell\nu J}$ and $p_T^J > 0.4 m_{\ell\nu J}$ cuts, which effectively enforce a $|\cos\theta^*| = 0.6$ maximum, as discussed before.

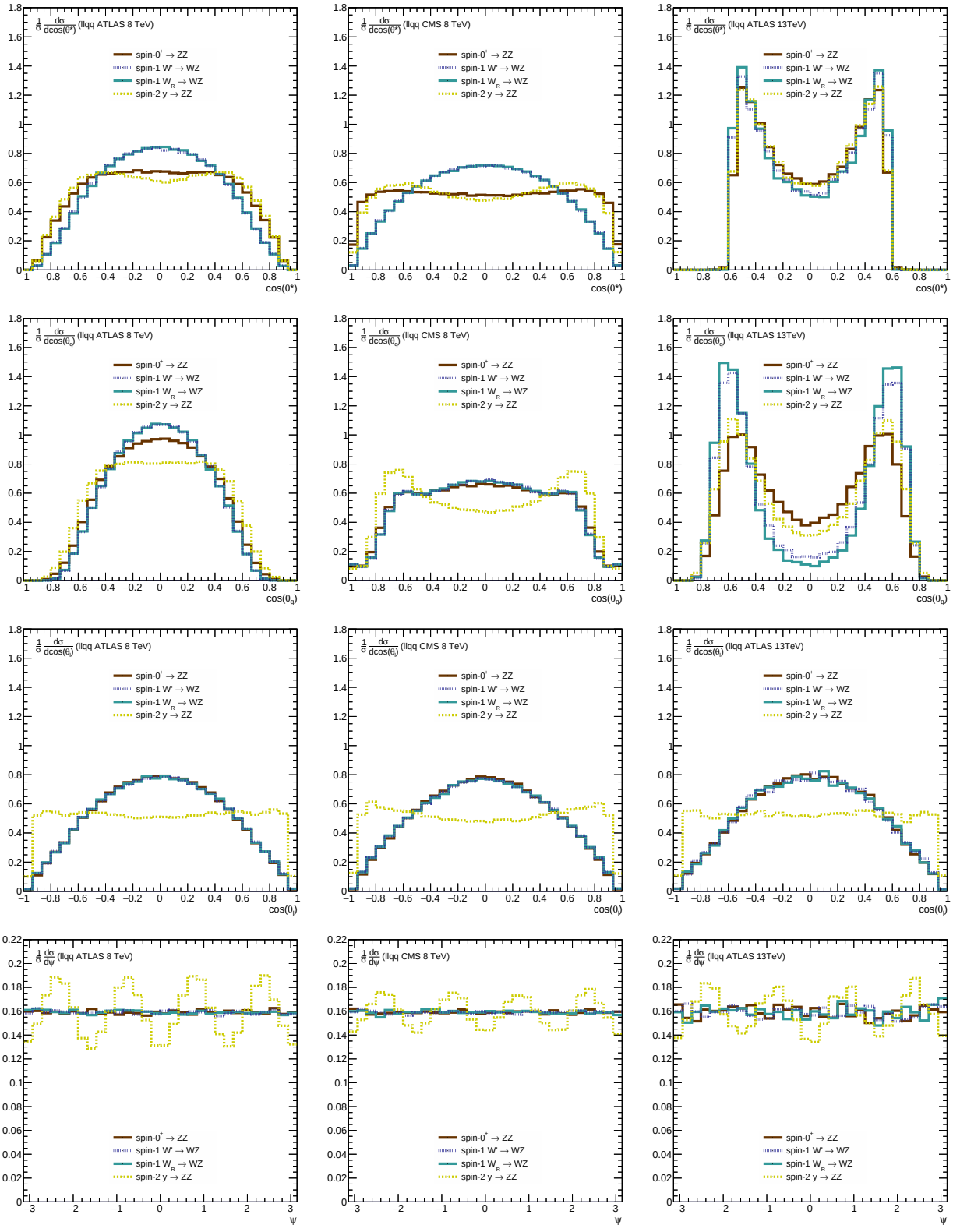

FIG. 9. Normalized differential distributions for $\cos\theta^*$ (top row), $\cos\theta_q$ (second row), $\cos\theta_l$ (third row), and Ψ (bottom row) angles in the semi-leptonic final state $\ell\ell qq$, after imposing the ATLAS 8 TeV (left column), CMS 8 TeV (middle), and ATLAS 13 TeV (right) analysis cuts.

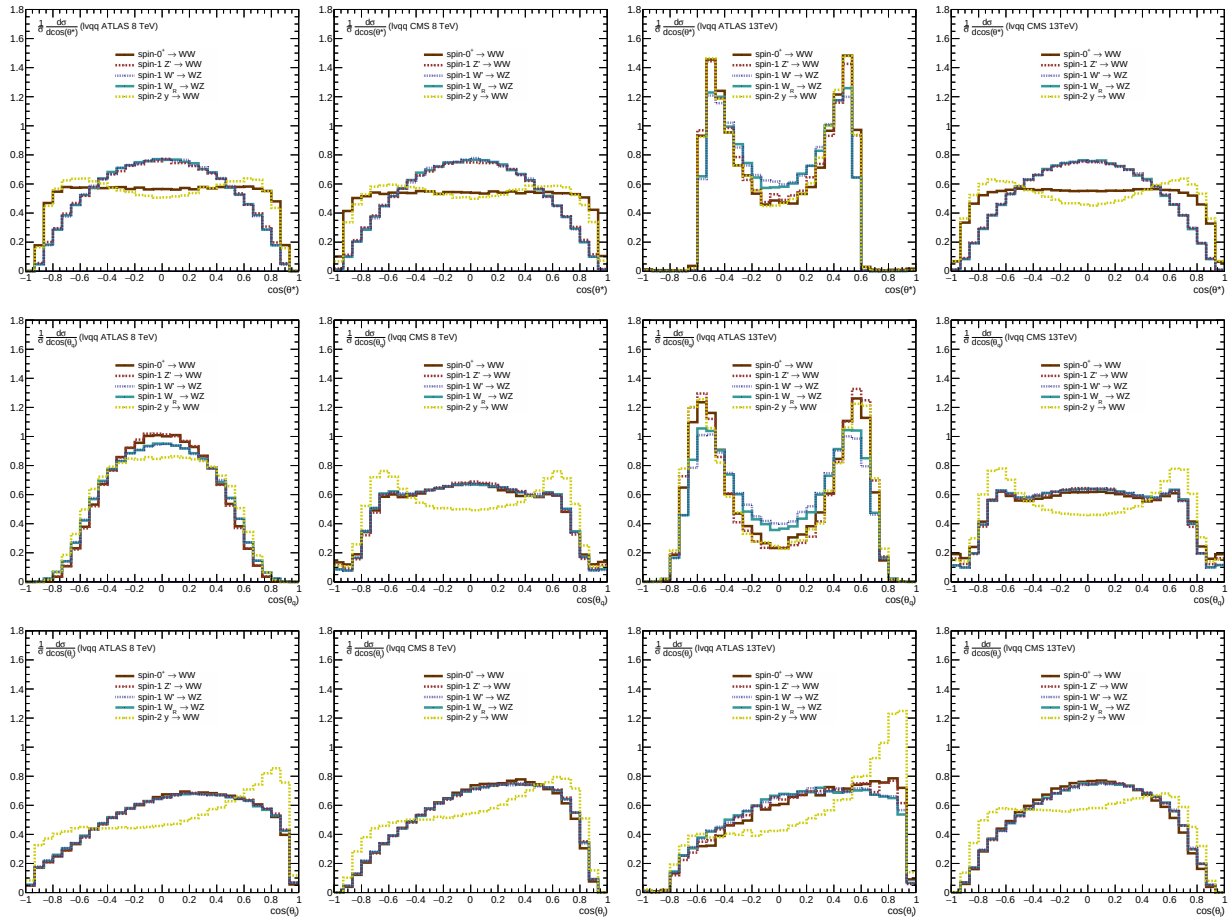

FIG. 10. Normalized differential distributions for $\cos\theta^*$ (top row), $\cos\theta_q$ (middle row), and $\cos\theta_l$ (bottom row), for the semi-leptonic final state $\ell\nu qq$, after imposing the ATLAS 8 TeV (first column), CMS 8 TeV (second column), ATLAS 13 TeV (third column), and CMS 13 TeV (last column) analysis cuts. We omit the Ψ angle as it does not have any significant discrimination power.

V. PROJECTIONS FOR MODEL DISCRIMINATION FROM $4q$ FINAL STATE

We now quantify the discrimination power between the different spin scenarios using the CL_s method [128] to test one signal against another in the $4q$ final state. We define one signal resonance plus dijet background as a signal hypothesis, whereas the test hypothesis is a different spin resonance plus the same dijet background. We use the differential shapes $|\cos\theta^*|$, $|\cos\theta_q|$, and $|\Psi|$ as individual discriminators as well as a likelihood combination using all three observables.

We perform the pairwise signal hypothesis tests first using shape information alone and second using both shape and rate information. The normalized differential distributions serve as a first test for signal comparisons, because, by construction, different models for a newly discovered resonance will have the same fiducial signal cross section in order to match the observed excess. Hence, even if the 2 TeV excess seen by ATLAS with 8 TeV data is not confirmed by the 13 TeV dataset, our shape-only spin comparisons are indicative of the expected performance of different observables at the initial discovery stage. On the other hand, if data from two different $\sqrt{s}$ working points is available, then the expected scaling from changes in parton distribution functions (PDFs) on various signal rates would be an additional handle to discriminate between models.

Since we adopt the ATLAS 2 TeV diboson excess as our case study, we first normalize the respective differential shapes to this excess. In a 300 GeV window centered at $m_{JJ} = 2$ TeV, the ATLAS collaboration observed an excess of 8 events over an expected background of 8.94 events [8], where we quote the inclusive diboson tagging requirements. We use this normalization factor, our simulated signal efficiencies, and our simulated PDF rescaling factors to determine the expected number of signal events for each of the other experimental analyses. In the shape only comparisons, the test hypothesis is always normalized to the null hypothesis. The corresponding background expectations, again for inclusive diboson selection cuts, are gleaned from each ATLAS and CMS analysis, albeit with slightly shifted mass windows around the X mass.[3] Since the current ATLAS 13 TeV analysis does not show event counts for an inclusive diboson selection, we estimate the inclusive background expectation from their available data, which we detail in Appendix A.

Not surprisingly, the current discrimination power between different resonance spins is low given the small signal statistics of the 8 TeV and 13 TeV analyses. This situation is expected to dramatically improve, however, with 30 fb^{-1} luminosity of 13 TeV data. In Fig. 11, we show the CL_s values for a given null hypothesis and various test hypotheses using the current ATLAS 13 TeV and CMS 13 TeV analyses [10, 11] rescaled for 30 fb^{-1} of luminosity. We assume a 25%

[3] We use the following invariant mass bins: $[1850, 2150]$ GeV for ATLAS at 8 TeV, $[1800, 2200]$ GeV for ATLAS at 13 TeV, and $[1852.3, 2136.4]$ GeV for CMS at 13 TeV.

systematic uncertainty on the signal, and 30% on the dijet background. In each row of each figure, the central exclusion limit using only differential distributions is shown as a solid black line, and the corresponding 68% and 95% expected C.L. exclusion limits are shown as the yellow and green bands. The dotted line in each row shows the shift in the central expected exclusion limit if rate information is also added in the signal hypothesis test. These C.L. results are not symmetric under interchange of null hypothesis and test hypotheses, because in the shapes-only CL_s analysis, the test hypothesis is always scaled to the null hypothesis, and thus the S/B measure is not equal under the interchange. When rates are included, the Poisson errors are not equal under interchange, and so the resulting C.L. expectations are again not equal.

We see that the most discrimination power comes between the spin-0 and spin-1 cases vs. the spin-2 case, which is expected from the clear distinctions in angular correlations from Fig. 2 for $\cos\theta^*$, Fig. 4 for $\cos\theta_q$, as well as Fig. 7 for Ψ. In particular, the $\cos\theta_q$ observable provides significant discrimination, as the spin-2 concavity in the reconstructed differential distribution is opposite that of the spin-0 and spin-1 resonances. We also remark that the $\cos\theta_q$ observable has twice the statistical power of the other $\cos\theta^*$ and Ψ distributions because each event gives two reconstructed vector boson candidates, and each vector boson candidate contributes one entry to the $\cos\theta_q$ distribution.

We also see that CMS generally has stronger projected sensitivity than ATLAS, which is a direct result of the different substructure analyses employed by each experiment. In particular, the ATLAS 13 TeV analysis clusters large radius anti-k_T jets with $R = 1.0$ and trims these jets using a k_T algorithm with $R = 0.2$ and hardness measure $z_{\min} = 0.05$. We have seen from Fig. 3 that the bulk of the quark pairs from $X \to VV \to 4q$ decays lie within $\Delta R = 0.2$, which causes many of the nominal subjets to be merged at the trimming stage.

As a result, the efficiency for the ATLAS 13 TeV analysis to identify two distinct subjets is significantly lower than the corresponding CMS 13 TeV analysis, causing the overall sensitivity to distinguishing spin hypotheses to suffer.

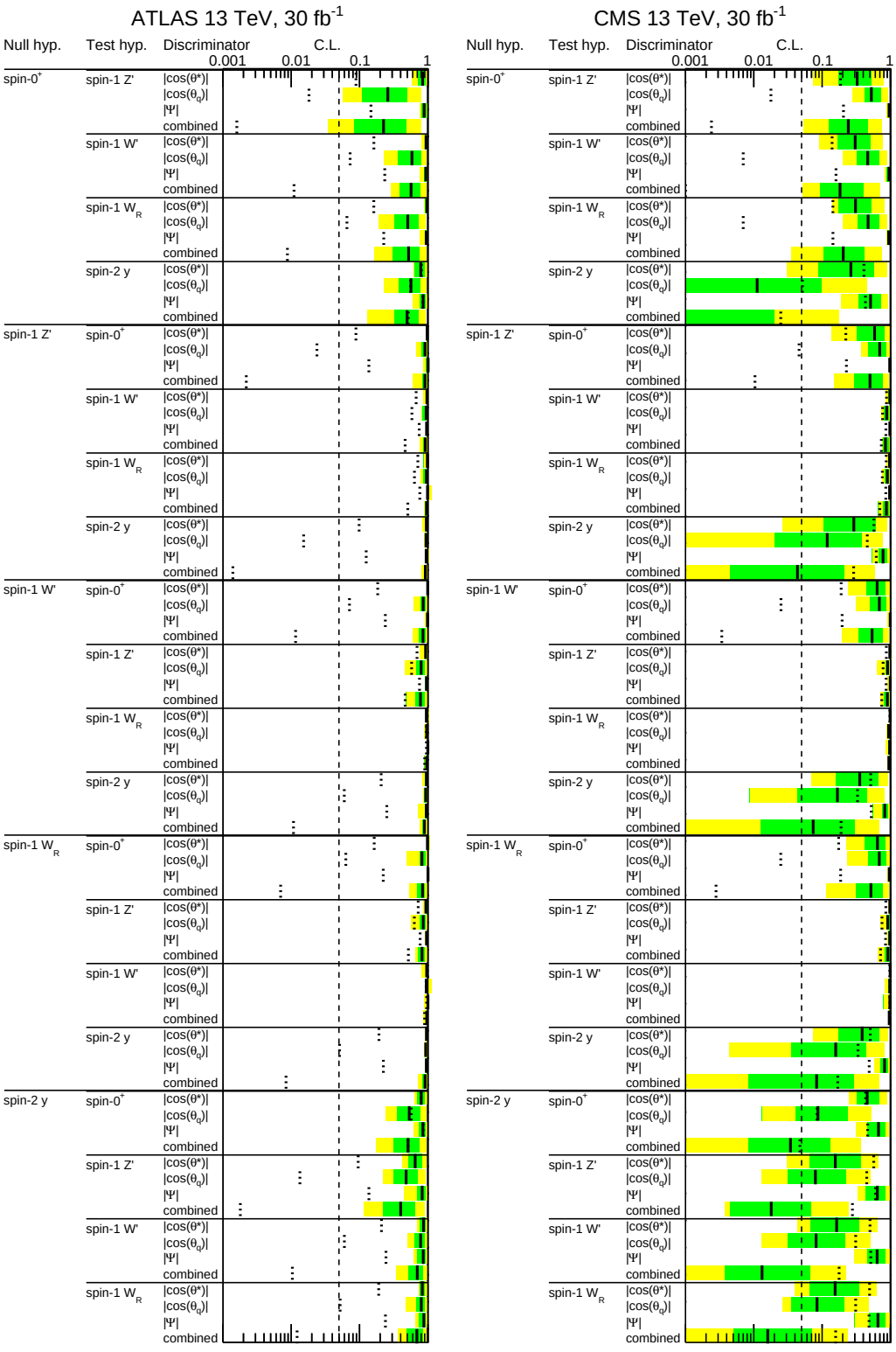

FIG. 11. Projected spin sensitivity for the 13 TeV ATLAS (left) and CMS (right) analyses with 30 fb^{-1} integrated luminosity. The long vertical dashed line indicates the 95% exclusion C.L. Within each row, the solid black line and the green and yellow shaded areas denote the central expected exclusion and the 68% and 95% likelihood expected exclusion intervals, using only shape information. The dotted black line in each row shows the central expected exclusion limit including rate information, using the 2 TeV excess as the normalization of the respective signal hypotheses.

The inclusion of rate information shows strong discrimination between the spin-0 null hypothesis compared to the spin-1 hypotheses. This simply follows from the fact that our ad-hoc, gluon-fusion induced, spin-0 diboson resonance enjoys a significant PDF rescaling factor when going from 8 TeV to 13 TeV. In contrast, the qq'-initiated Z', W', and W_R spin-1 signals are all largely indistinguishable when only considering the $4q$ final state. All of these spin-1 bosons couple to the SM electroweak bosons using the same tree-level Lagrangian structure, which makes it very difficult to disentangle by only considering the $4q$ excess. The small sensitivity afforded by shape and rate information in distinguishing a Z' from a W' or W_R explanation comes from the different PDF scaling from 8 TeV to 13 TeV between qq' vs. $q\bar{q}$ initial states. We also note that our signal and background events use inclusive WW, WZ, and ZZ hadronic diboson tags, and thus additional sensitivity to W' or W_R discrimination from a Z' signal would come from separating these diboson tagging categories.

In some cases, however, the inclusion of rate information decreases the overall discrimination power between signal hypotheses. This is because the shapes-only test magnifies the importance of low event count bins where the signal to background ratio is high, whereas the shapes and rates test loses discrimination power by having an overall lower significance for the given signals. In particular, the linear rescaling we use for matching the signal rates in the rates-only tests overcomes the Poisson statistics governing the low-count bins that is otherwise dominant in the rates and shapes test.

Overall, we see that the spin-2 signal hypothesis will be tested at 95% C.L. using CMS 13 TeV cuts with 30 fb^{-1} luminosity. We also project 95% C.L. sensitivity between spin-0 and other spin scenarios by combining rate information with the differential distributions. If a new diboson resonance appears, however, the shape information alone from the current 13 TeV analyses would be insufficient to distinguish spin-0 from spin-1 possibilities.

We conclude this section by discussing the possible improvements to jet substructure analyses that could significantly help the prospects of signal discrimination in a fully hadronic diboson final state. We have seen how the maximum $\Delta\eta_{JJ}$ cut introduces cliffs in $\cos\theta^*$ that significantly cut away parts of phase space that would tell a spin-1 signal from other possibilities. Allowing a looser $\Delta\eta_{JJ}$ cut, up to $\Delta\eta_{JJ} \leq 2.2$, for example, would ensure that the extra sinuisoidal oscillation in the spin-2 hypothesis would be more easily distinguished compared to the spin-0 hypothesis and the dijet background, as seen in Fig. 2. Although such a loose cut would lead to an immense increase in multijet background, even intermediate values of $\Delta\eta_{JJ} > 1.3$ would already aid discrimination power between the different spin hypotheses. We have also seen that the minimum subjet p_T

balance requirement removes events above $|\cos\theta_q| \approx 0.66$–$0.90$, depending on the $y_{\min}$ cut. These events would have the best discrimination power between spin-2 signals and other possibilities.

The most pernicious effect, however, comes from using a hard angular scale, such as the k_T reclustering with $R = 0.2$ inherent in the trimming procedure used by ATLAS 13 TeV analysis. This hard angular scale not only causes distinct parton-level decays to merge into single subjets, it also quashes the viability of a post-discovery analysis that builds angular correlations from multiple subjets and introduces significant sculpting effects in $\cos\theta^*$ and $\cos\theta_q$ distributions. For our 2 TeV case study, the efficiency to find four distinct subjets would increase significantly if a smaller reclustering radius of $R = 0.15$ were used, as seen in Figure 3, but the minimum radius for a given resonance mass hypothesis with mass m_X can be estimated from $R_{\min} \lesssim 2m_{W/Z}/p_{T,X} \sim m_{W/Z}/m_X$.

A jet substructure method optimized for both signal discovery and post-discovery signal discrimination would ameliorate these negative effects. The subjet p_T balance requirement and alternate reclustering methods that do not introduce a hard angular scale are thus the most motivated details to modify for a spin-sensitive jet substructure optimization. We reserve a study to address these questions for future work.

VI. CONCLUSION

We have performed a comprehensive study of how angular correlations in resonance decays to four quarks can be preserved, albeit distorted, after effects from hadronization and showering, detector resolution, jet clustering, and W and Z tagging via currently employed jet substructure techniques. We have connected the observed cliffs in $\cos\theta^*$ to cuts on the maximum pseudorapidity difference between the parent fat jets, the deficit of events around $\cos\theta^*, \cos\theta_q \approx 0$ to the hard angular scale used in the reclustering of subjets, and the removal of events above $\cos\theta_q \approx 0.66$–$0.90$ to the subjet p_T balance requirement employed by the various analyses. We have also emphasized the importance of small angular scales for jet substructure reclustering, having seen how large reclustering radii merge distinct decay products of highly boosted vector parents and resulting sensitivity to spin discrimination is greatly reduced.

We recognize that spin discrimination of a new resonance in diboson decays is one facet of a possible post-discovery signal characterization effort. In particular, some of the degeneracies among the various spin-1 signal hypotheses can only be distinguished by observing semi-leptonic diboson decays as well as additional direct decays to fermions. The rates for the latter decays are model

dependent features of each given signal hypothesis. In the special case of the 2 TeV excess seen by ATLAS in 8 TeV data, additional discrimination power between possible new physics resonances is afforded by the simple fact that the LHC is now operating at 13 TeV. The different production modes for spin-0, spin-1 neutral, spin-1 charged, and spin-2 resonances obviously scale differently going from $\sqrt{s} = 8$ TeV to $\sqrt{s} = 13$ TeV, which establishes benchmark expected significances for the different signals as a function of luminosity.

Our work, however, addresses the more general question about the feasibility of using an analysis targetting a resonance in a fully hadronic diboson decay for spin and parity discrimination. It also provides a method for distinguishing longitudinal versus transverse polarizations of electroweak gauge bosons, which is an intrinsic element of analyses aimed at probing unitarity of electroweak boson scattering. A future work will tackle the question of an optimized jet substructure analysis that avoids introducing significant distortions in angular observables and hence enhances the possible spin sensitivity beyond the projections shown in Fig. 11. We also plan to investigate angular correlations in fully hadronic final states with intermediate new physics resonances, as well as the viability of angular observables using Higgs and top substructure methods. Even without any improvement, a spin-2 explanation for the 2 TeV excess will be tested at the 95% C.L. from other spin hypotheses with 30 fb^{-1} of 13 TeV luminosity using only shape information, while spin-0 vs. spin-1 discrimination would come from the combination of rate and shape information.

ACKNOWLEDGMENTS

We would like to thank Michael Baker, Ian Lewis, Adam Martin, Jesse Thaler, Andrea Thamm, Nhan Tran, and Yuhsin Tsai, for useful discussions, and Riccardo Torre, Andrea Thamm for use of the Heavy Vector Triplets FeynRules model and Bogdan Dobrescu and Patrick Fox for use of the right-handed W_R model. This research is supported by the Cluster of Excellence Precision Physics, Fundamental Interactions and Structure of Matter (PRISMA-EXC 1098). The work of MB is moreover supported by the German Research Foundation (DFG) in the framework of the Research Unit New Physics at the Large Hadron Collider" (FOR 2239).

Appendix A: ATLAS 13 TeV background extraction, inclusive diboson selection

For our projections on spin sensitivity at 13 TeV LHC, we require the background estimate for inclusive diboson selection cuts. As the current ATLAS 13 TeV analysis [10] only provides WW,

WZ, and ZZ event counts, which are not exclusive selection bins because of overlapping W and Z mass windows, we extract the inclusive number of events as follows.

For the mass range 1.0 TeV $< m_{JJ} <$ 2.5 TeV, the ATLAS analysis specifies that 38 events lie in the overlap region and contribute to all three channels. We thus assign $p \approx \sqrt{38/N}$ as a flat probability for an event with a W-tag to also be a Z-tagged event and vice versa, where N is the number of events passing inclusive diboson tagging requirements. We can write $N = N_{W^0Z^0} + N_{W^0W^0} + N_{Z^0Z^0}$, where each category is defined exclusively and without overlap. Then,

$$\begin{aligned} N = {} & N_{WZ} + N_{WW} + N_{ZZ} \\ & - N_{W^0Z^0} \cdot [\mathcal{P}(Z \text{ in overlap region}) + \mathcal{P}(W \text{ in overlap region}) + 2\mathcal{P}(W \text{ and } Z \text{ in overlap region})] \\ & - N_{W^0W^0} \cdot [\mathcal{P}(\text{one } W \text{ in overlap region}) + 2\mathcal{P}(\text{both } W \text{ in overlap region})] \\ & - N_{Z^0Z^0} \cdot [\mathcal{P}(\text{one } Z \text{ in overlap region}) + 2\mathcal{P}(\text{both } Z \text{ in overlap region})] \ , \end{aligned} \tag{A1}$$

where factors of 2 in Eq. A1 reflect the fact that this particular event contributes to all three categories and therefore two events need to be subtracted from the total sum. From the ATLAS analysis [10], we have $N_{WZ} + N_{WW} + N_{ZZ} = 300$, thus

$$\begin{aligned} N &= 300 - N_{W^0Z^0}\left[p(1-p) + p(1-p) + 2p^2\right] \\ &\quad - N_{W^0W^0}\left[2p(1-p) + 2p^2\right] \\ &\quad - N_{Z^0Z^0}\left[2p(1-p) + 2p^2\right] \\ &= 300 - 2Np \ . \end{aligned} \tag{A2}$$

Using $p \approx \sqrt{38/N}$, and solving for N, we obtain $N \approx 149$, and thus 75 events fall into two diboson categories and 38 events are triply counted, which is very similar to the breakdown of double and triple counted events in the ATLAS 8 TeV analysis [8]. We use this fraction to estimate the expected number of background events passing the inclusive diboson tagging requirements.

---

[1] J. M. Butterworth, A. R. Davison, M. Rubin, and G. P. Salam, Phys. Rev. Lett. **100**, 242001 (2008), arXiv:0802.2470 [hep-ph].

[2] A. Abdesselam *et al.*, *Boost 2010 Oxford, United Kingdom, June 22-25, 2010*, Eur. Phys. J. **C71**, 1661 (2011), arXiv:1012.5412 [hep-ph].

[3] A. Altheimer *et al.*, *BOOST 2011 Princeton , NJ, USA, 2226 May 2011*, J. Phys. **G39**, 063001 (2012), arXiv:1201.0008 [hep-ph].

[4] A. Altheimer *et al.*, *BOOST 2012 Valencia, Spain, July 23-27, 2012*, Eur. Phys. J. **C74**, 2792 (2014), arXiv:1311.2708 [hep-ex].

[5] D. Adams *et al.*, Eur. Phys. J. **C75**, 409 (2015), arXiv:1504.00679 [hep-ph].

[6] G. Aad *et al.* (ATLAS), JHEP **05**, 128 (2012), arXiv:1203.4606 [hep-ex].

[7] G. Aad *et al.* (ATLAS), JHEP **09**, 076 (2013), arXiv:1306.4945 [hep-ex].

[8] G. Aad *et al.* (ATLAS), (2015), arXiv:1506.00962 [hep-ex].

[9] V. Khachatryan *et al.* (CMS), JHEP **08**, 173 (2014), arXiv:1405.1994 [hep-ex].

[10] *Search for resonances with boson-tagged jets in 3.2 fb1 of p p collisions at $\sqrt{s}$ = 13 TeV collected with the ATLAS detector*, Tech. Rep. ATLAS-CONF-2015-073 (CERN, Geneva, 2015).

[11] *Search for massive resonances decaying into pairs of boosted W and Z bosons at $\sqrt{s}$ = 13 TeV*, Tech. Rep. CMS-PAS-EXO-15-002 (CERN, Geneva, 2015).

[12] G. Aad *et al.* (ATLAS), Phys. Lett. **B737**, 223 (2014), arXiv:1406.4456 [hep-ex].

[13] G. Aad *et al.* (ATLAS), Eur. Phys. J. **C75**, 69 (2015), arXiv:1409.6190 [hep-ex].

[14] G. Aad *et al.* (ATLAS), Eur. Phys. J. **C75**, 209 (2015), [Erratum: Eur. Phys. J.C75,370(2015)], arXiv:1503.04677 [hep-ex].

[15] G. Aad *et al.* (ATLAS), (2015), arXiv:1512.05099 [hep-ex].

[16] V. Khachatryan *et al.* (CMS), Phys. Lett. **B740**, 83 (2015), arXiv:1407.3476 [hep-ex].

[17] V. Khachatryan *et al.* (CMS), JHEP **08**, 174 (2014), arXiv:1405.3447 [hep-ex].

[18] J. Brehmer *et al.*, (2015), arXiv:1512.04357 [hep-ph].

[19] *Search for WW/WZ resonance production in the $\ell\nu qq$ final state at $\sqrt{s} = 13$ TeV with the ATLAS detector at the LHC*, Tech. Rep. ATLAS-CONF-2015-075 (CERN, Geneva, 2015).

[20] *Search for diboson resonances in the llqq final state in pp collisions at $\sqrt{s}$ = 13 TeV with the ATLAS detector*, Tech. Rep. ATLAS-CONF-2015-071 (CERN, Geneva, 2015).

[21] *Search for diboson resonances in the $\nu\nu qq$ final state in pp collisions at $\sqrt{s}$ =13 TeV with the ATLAS detector*, Tech. Rep. ATLAS-CONF-2015-068 (CERN, Geneva, 2015).

[22] B. A. Dobrescu and Z. Liu, Phys. Rev. Lett. **115**, 211802 (2015), arXiv:1506.06736 [hep-ph].

[23] B. A. Dobrescu and Z. Liu, JHEP **10**, 118 (2015), arXiv:1507.01923 [hep-ph].

[24] J. Brehmer, J. Hewett, J. Kopp, T. Rizzo, and J. Tattersall, JHEP **10**, 182 (2015), arXiv:1507.00013 [hep-ph].

[25] B. A. Dobrescu and P. J. Fox, (2015), arXiv:1511.02148 [hep-ph].

[26] L. A. Anchordoqui, I. Antoniadis, H. Goldberg, X. Huang, D. Lust, and T. R. Taylor, Phys. Lett. **B749**, 484 (2015), arXiv:1507.05299 [hep-ph].

[27] G. Aad *et al.* (ATLAS), Phys. Rev. **D91**, 052007 (2015), arXiv:1407.1376 [hep-ex].

[28] V. Khachatryan *et al.* (CMS), Phys. Rev. **D91**, 052009 (2015), arXiv:1501.04198 [hep-ex].

[29] G. Aad *et al.* (ATLAS), Phys. Lett. **B754**, 302 (2016), [Phys. Lett.B754,302(2016)], arXiv:1512.01530 [hep-ex].

[30] V. Khachatryan *et al.* (CMS), (2015), arXiv:1512.01224 [hep-ex].

[31] G. Aad *et al.* (ATLAS), Eur. Phys. J. **C75**, 263 (2015), arXiv:1503.08089 [hep-ex].

[32] V. Khachatryan *et al.* (CMS), Phys. Lett. **B748**, 255 (2015), arXiv:1502.04994 [hep-ex].

[33] V. Khachatryan *et al.* (CMS), (2015), arXiv:1506.01443 [hep-ex].

[34] V. Khachatryan *et al.* (CMS), (2016), arXiv:1601.06431 [hep-ex].

[35] *Search for new resonances decaying to a W or Z boson and a Higgs boson in the $\ell\ell b\bar{b}$, $\ell\nu b\bar{b}$, and $\nu\nu b\bar{b}$ channels in pp collisions at $\sqrt{s} = 13$ TeV with the ATLAS detector*, Tech. Rep. ATLAS-CONF-2015-074 (CERN, Geneva, 2015).

[36] C.-H. Chen and T. Nomura, (2015), arXiv:1509.02039 [hep-ph].

[37] C.-H. Chen and T. Nomura, Phys. Lett. **B749**, 464 (2015), arXiv:1507.04431 [hep-ph].

[38] Y. Omura, K. Tobe, and K. Tsumura, Phys. Rev. **D92**, 055015 (2015), arXiv:1507.05028 [hep-ph].

[39] W. Chao, (2015), arXiv:1507.05310 [hep-ph].

[40] D. Aristizabal Sierra, J. Herrero-Garcia, D. Restrepo, and A. Vicente, (2015), arXiv:1510.03437 [hep-ph].

[41] C. Petersson and R. Torre, (2015), arXiv:1508.05632 [hep-ph].

[42] B. C. Allanach, P. S. B. Dev, and K. Sakurai, (2015), arXiv:1511.01483 [hep-ph].

[43] C.-W. Chiang, H. Fukuda, K. Harigaya, M. Ibe, and T. T. Yanagida, JHEP **11**, 015 (2015), arXiv:1507.02483 [hep-ph].

[44] G. Cacciapaglia, A. Deandrea, and M. Hashimoto, Phys. Rev. Lett. **115**, 171802 (2015), arXiv:1507.03098 [hep-ph].

[45] H. S. Fukano, M. Kurachi, S. Matsuzaki, K. Terashi, and K. Yamawaki, Phys. Lett. **B750**, 259 (2015), arXiv:1506.03751 [hep-ph].

[46] D. B. Franzosi, M. T. Frandsen, and F. Sannino, (2015), arXiv:1506.04392 [hep-ph].

[47] A. Thamm, R. Torre, and A. Wulzer, Phys. Rev. Lett. **115**, 221802 (2015), arXiv:1506.08688 [hep-ph].

[48] L. Bian, D. Liu, and J. Shu, (2015), arXiv:1507.06018 [hep-ph].

[49] H. Fritzsch, (2015), arXiv:1507.06499 [hep-ph].

[50] K. Lane and L. Prichett, (2015), arXiv:1507.07102 [hep-ph].

[51] M. Low, A. Tesi, and L.-T. Wang, Phys. Rev. **D92**, 085019 (2015), arXiv:1507.07557 [hep-ph].

[52] H. S. Fukano, S. Matsuzaki, K. Terashi, and K. Yamawaki, (2015), arXiv:1510.08184 [hep-ph].

[53] G. Cacciapaglia and M. T. Frandsen, Phys. Rev. **D92**, 055035 (2015), arXiv:1507.00900 [hep-ph].

[54] B. C. Allanach, B. Gripaios, and D. Sutherland, Phys. Rev. **D92**, 055003 (2015), arXiv:1507.01638 [hep-ph].

[55] L. Bian, D. Liu, J. Shu, and Y. Zhang, (2015), arXiv:1509.02787 [hep-ph].

[56] B. Bhattacherjee, P. Byakti, C. K. Khosa, J. Lahiri, and G. Mendiratta, (2015), arXiv:1511.02797 [hep-ph].

[57] S.-S. Xue, (2015), arXiv:1506.05994 [hep-ph].

[58] Y. Gao, T. Ghosh, K. Sinha, and J.-H. Yu, Phys. Rev. **D92**, 055030 (2015), arXiv:1506.07511 [hep-ph].

[59] J. Heeck and S. Patra, Phys. Rev. Lett. **115**, 121804 (2015), arXiv:1507.01584 [hep-ph].

[60] P. S. Bhupal Dev and R. N. Mohapatra, Phys. Rev. Lett. **115**, 181803 (2015), arXiv:1508.02277 [hep-ph].

[61] F. F. Deppisch, L. Graf, S. Kulkarni, S. Patra, W. Rodejohann, N. Sahu, and U. Sarkar, (2015), arXiv:1508.05940 [hep-ph].

[62] U. Aydemir, D. Minic, C. Sun, and T. Takeuchi, (2015), arXiv:1509.01606 [hep-ph].

[63] R. L. Awasthi, P. S. B. Dev, and M. Mitra, (2015), arXiv:1509.05387 [hep-ph].

[64] P. Ko and T. Nomura, (2015), arXiv:1510.07872 [hep-ph].

[65] J. H. Collins and W. H. Ng, (2015), arXiv:1510.08083 [hep-ph].

[66] J. A. Aguilar-Saavedra and F. R. Joaquim, (2015), arXiv:1512.00396 [hep-ph].

[67] U. Aydemir, Int. J. Mod. Phys. **A31**, 1650034 (2016), arXiv:1512.00568 [hep-ph].

[68] J. L. Evans, N. Nagata, K. A. Olive, and J. Zheng, (2015), arXiv:1512.02184 [hep-ph].

[69] A. Das, N. Nagata, and N. Okada, JHEP **03**, 049 (2016), arXiv:1601.05079 [hep-ph].

[70] J. Hisano, N. Nagata, and Y. Omura, Phys. Rev. **D92**, 055001 (2015), arXiv:1506.03931 [hep-ph].

[71] A. Alves, A. Berlin, S. Profumo, and F. S. Queiroz, JHEP **10**, 076 (2015), arXiv:1506.06767 [hep-ph].

[72] A. E. Faraggi and M. Guzzi, Eur. Phys. J. **C75**, 537 (2015), arXiv:1507.07406 [hep-ph].

[73] T. Li, J. A. Maxin, V. E. Mayes, and D. V. Nanopoulos, (2015), arXiv:1509.06821 [hep-ph].

[74] Z.-W. Wang, F. S. Sage, T. G. Steele, and R. B. Mann, (2015), arXiv:1511.02531 [hep-ph].

[75] B. Allanach, F. S. Queiroz, A. Strumia, and S. Sun, (2015), arXiv:1511.07447 [hep-ph].

[76] W.-Z. Feng, Z. Liu, and P. Nath, (2015), arXiv:1511.08921 [hep-ph].

[77] K. Cheung, W.-Y. Keung, P.-Y. Tseng, and T.-C. Yuan, Phys. Lett. **B751**, 188 (2015), arXiv:1506.06064 [hep-ph].

[78] Q.-H. Cao, B. Yan, and D.-M. Zhang, Phys. Rev. **D92**, 095025 (2015), arXiv:1507.00268 [hep-ph].

[79] T. Abe, R. Nagai, S. Okawa, and M. Tanabashi, Phys. Rev. **D92**, 055016 (2015), arXiv:1507.01185 [hep-ph].

[80] T. Abe, T. Kitahara, and M. M. Nojiri, (2015), arXiv:1507.01681 [hep-ph].

[81] H. S. Fukano, S. Matsuzaki, and K. Yamawaki, (2015), arXiv:1507.03428 [hep-ph].

[82] T. Appelquist, Y. Bai, J. Ingoldby, and M. Piai, (2015), arXiv:1511.05473 [hep-ph].

[83] K. Das, T. Li, S. Nandi, and S. K. Rai, (2015), arXiv:1512.00190 [hep-ph].

[84] V. Sanz, (2015), arXiv:1507.03553 [hep-ph].

[85] H. Terazawa and M. Yasue, (2015), arXiv:1508.00172 [hep-ph].

[86] J. A. Aguilar-Saavedra, JHEP **10**, 099 (2015), arXiv:1506.06739 [hep-ph].

[87] D. Kim, K. Kong, H. M. Lee, and S. C. Park, (2015), arXiv:1507.06312 [hep-ph].

[88] S. P. Liew and S. Shirai, JHEP **11**, 191 (2015), arXiv:1507.08273 [hep-ph].

[89] P. Arnan, D. Espriu, and F. Mescia, (2015), arXiv:1508.00174 [hep-ph].

[90] S. Fichet and G. von Gersdorff, (2015), arXiv:1508.04814 [hep-ph].

[91] A. Sajjad, (2015), arXiv:1511.02244 [hep-ph].

[92] G. Aad *et al.* (ATLAS), Eur. Phys. J. **C75**, 476 (2015), arXiv:1506.05669 [hep-ex].

[93] G. Aad *et al.* (ATLAS), Eur. Phys. J. **C76**, 6 (2016), arXiv:1507.04548 [hep-ex].

[94] V. Khachatryan *et al.* (CMS), Phys. Rev. **D92**, 012004 (2015), arXiv:1411.3441 [hep-ex].

[95] V. Khachatryan *et al.* (CMS), Eur. Phys. J. **C75**, 212 (2015), arXiv:1412.8662 [hep-ex].

[96] N. Cabibbo and A. Maksymowicz, Phys. Rev. **137**, B438 (1965), [Erratum: Phys. Rev.168,1926(1968)].

[97] J. R. Dell'Aquila and C. A. Nelson, Phys. Rev. **D33**, 80 (1986).

[98] J. R. Dell'Aquila and C. A. Nelson, Phys. Rev. **D33**, 93 (1986).

[99] C. A. Nelson, *Proceedings, 23RD International Conference on High Energy Physics, JULY 16-23, 1986, Berkeley, CA*, Phys. Rev. **D37**, 1220 (1988).

[100] Y. Gao, A. V. Gritsan, Z. Guo, K. Melnikov, M. Schulze, and N. V. Tran, Phys. Rev. **D81**, 075022 (2010), arXiv:1001.3396 [hep-ph].

[101] S. Bolognesi, Y. Gao, A. V. Gritsan, K. Melnikov, M. Schulze, N. V. Tran, and A. Whitbeck, Phys. Rev. **D86**, 095031 (2012), arXiv:1208.4018 [hep-ph].

[102] Y. Chen, N. Tran, and R. Vega-Morales, JHEP **01**, 182 (2013), arXiv:1211.1959 [hep-ph].

[103] Y. Chen, E. Di Marco, J. Lykken, M. Spiropulu, R. Vega-Morales, and S. Xie, JHEP **01**, 125 (2015), arXiv:1401.2077 [hep-ex].

[104] Y. Chen, E. Di Marco, J. Lykken, M. Spiropulu, R. Vega-Morales, and S. Xie, (2014), arXiv:1410.4817 [hep-ph].

[105] Y. L. Dokshitzer, G. D. Leder, S. Moretti, and B. R. Webber, JHEP **08**, 001 (1997), arXiv:hep-ph/9707323 [hep-ph].

[106] S. D. Ellis, C. K. Vermilion, and J. R. Walsh, Phys. Rev. **D80**, 051501 (2009), arXiv:0903.5081 [hep-ph].

[107] S. D. Ellis, C. K. Vermilion, and J. R. Walsh, Phys. Rev. **D81**, 094023 (2010), arXiv:0912.0033 [hep-ph].

[108] J. Thaler and K. Van Tilburg, JHEP **03**, 015 (2011), arXiv:1011.2268 [hep-ph].

[109] J. Thaler and K. Van Tilburg, JHEP **02**, 093 (2012), arXiv:1108.2701 [hep-ph].

[110] D. Krohn, J. Thaler, and L.-T. Wang, JHEP **02**, 084 (2010), arXiv:0912.1342 [hep-ph].

[111] S. Catani, Y. L. Dokshitzer, M. H. Seymour, and B. R. Webber, Nucl. Phys. **B406**, 187 (1993).

[112] A. J. Larkoski, G. P. Salam, and J. Thaler, JHEP **06**, 108 (2013), arXiv:1305.0007 [hep-ph].

[113] A. J. Larkoski, I. Moult, and D. Neill, JHEP **12**, 009 (2014), arXiv:1409.6298 [hep-ph].

[114] A. J. Larkoski, I. Moult, and D. Neill, (2015), arXiv:1507.03018 [hep-ph].

[115] A. Alloul, N. D. Christensen, C. Degrande, C. Duhr, and B. Fuks, Comput. Phys. Commun. **185**, 2250 (2014), arXiv:1310.1921 [hep-ph].

[116] J. Alwall, M. Herquet, F. Maltoni, O. Mattelaer, and T. Stelzer, JHEP **06**, 128 (2011), arXiv:1106.0522 [hep-ph].

[117] D. Pappadopulo, A. Thamm, R. Torre, and A. Wulzer, JHEP **09**, 060 (2014), arXiv:1402.4431 [hep-ph].

[118] L. Randall and R. Sundrum, Phys. Rev. Lett. **83**, 3370 (1999), arXiv:hep-ph/9905221 [hep-ph].

[119] L. Randall and R. Sundrum, Phys. Rev. Lett. **83**, 4690 (1999), arXiv:hep-th/9906064 [hep-th].

[120] K. Hagiwara, J. Kanzaki, Q. Li, and K. Mawatari, Eur. Phys. J. **C56**, 435 (2008), arXiv:0805.2554 [hep-ph].

[121] T. Sjstrand, S. Ask, J. R. Christiansen, R. Corke, N. Desai, P. Ilten, S. Mrenna, S. Prestel, C. O. Rasmussen, and P. Z. Skands, Comput. Phys. Commun. **191**, 159 (2015), arXiv:1410.3012 [hep-ph].

[122] J. de Favereau, C. Delaere, P. Demin, A. Giammanco, V. Lematre, A. Mertens, and M. Selvaggi (DELPHES 3), JHEP **02**, 057 (2014), arXiv:1307.6346 [hep-ex].

[123] M. Cacciari, G. P. Salam, and G. Soyez, Eur. Phys. J. **C72**, 1896 (2012), arXiv:1111.6097 [hep-ph].

[124] M. Cacciari, G. P. Salam, and G. Soyez, JHEP **04**, 063 (2008), arXiv:0802.1189 [hep-ph].

[125] V. Khachatryan *et al.* (CMS), JHEP **12**, 017 (2014), arXiv:1410.4227 [hep-ex].

[126] C. Hackstein and M. Spannowsky, Phys. Rev. **D82**, 113012 (2010), arXiv:1008.2202 [hep-ph].

[127] C. Englert, C. Hackstein, and M. Spannowsky, Phys. Rev. **D82**, 114024 (2010), arXiv:1010.0676 [hep-ph].

[128] A. L. Read, *Advanced Statistical Techniques in Particle Physics. Proceedings, Conference, Durham, UK, March 18-22, 2002*, J. Phys. **G28**, 2693 (2002), [,11(2002)].